

A Semiautomated Multilayer Picking Algorithm for Ice-Sheet Radar Echograms Applied to Ground-Based Near-Surface Data

Vincent de Paul Onana, Lora S. Koenig, Julia Ruth, Michael Studinger, and Jeremy P. Harbeck

Abstract—Snow accumulation over an ice sheet is the sole mass input, making it a primary measurement for understanding the past, present, and future mass balance. Near-surface frequency-modulated continuous-wave (FMCW) radars image isochronous firn layers recording accumulation histories. The Semiautomated Multilayer Picking Algorithm (SAMPA) was designed and developed to trace annual accumulation layers in polar firn from both airborne and ground-based radars. The SAMPA algorithm is based on the Radon transform (RT) computed by blocks and angular orientations over a radar echogram. For each echogram's block, the RT maps firn segmented-layer features into peaks, which are picked using amplitude and width threshold parameters of peaks. A backward RT is then computed for each corresponding block, mapping the peaks back into picked segmented-layers. The segmented layers are then connected and smoothed to achieve a final layer pick across the echogram. Once input parameters are trained, SAMPA operates autonomously and can process hundreds of kilometers of radar data picking more than 40 layers. SAMPA final pick results and layer numbering still require a cursory manual adjustment to correct noncontinuous picks, which are likely not annual, and to correct for inconsistency in layer numbering. Despite the manual effort to train and check SAMPA results, it is an efficient tool for picking multiple accumulation layers in polar firn, reducing time over manual digitizing efforts. The trackability of good detected layers is greater than 90%.

Index Terms—Antarctic ice sheet, image transforms, layers' trackability, radar echo sounding, Radon transform (RT).

I. INTRODUCTION

RADAR echo sounding of the ice sheets is and has been an active area of glaciological research, e.g., [1] and [2]. When a radar wave penetrates an ice sheet, the physical and

chemical properties of the firn reflect, refract, and attenuate the wave, creating an image of the internal structure (e.g., [3], vol II; [2]). Radar echograms have been used extensively to map the underlying bedrock of ice sheets, to determine past ice-flow histories and to determine accumulation rates, e.g., [4]–[8]. With the start of NASA's Operation IceBridge in 2009, an unprecedented amount of new depth-sounding and near-surface radar data have been collected, and there is great need for automated and/or semiautomated algorithms for detecting and mapping isochronal layers in these data (e.g., [9] and [10]). There is particular need for automated methods that can resolve annual accumulation rates from the high-resolution and frequency-modulated continuous-wave (FMCW) radars that image the near-surface (\approx top 20–80 m) firn across the ice sheets (e.g., [11], [12]). Snow accumulation is the sole input to ice-sheet mass balance and is thus a necessary input for monitoring ice-sheet contributions to sea level rise. Reanalysis and regional atmospheric models are most commonly used to investigate changes in spatial and temporal variation in accumulation across ice sheets but are largely unchecked by measurements (e.g., [13]–[18]). Spatially and temporally extensive radar-derived measurements of accumulation are extremely important due to the paucity of accumulation measurements from ice cores and snow pits and the lack of a reliable annually resolved satellite retrieval of accumulation (e.g., [19]–[21]).

Here, we present a first step toward retrieving spatially and temporally extensive maps of accumulation from radar measurements by introducing the Semiautomated Multilayer Picking Algorithm (SAMPA). SAMPA uses image-processing techniques to trace and extract firn layers in near-surface radar echograms. Layer extraction results are shown, along with a comparison of extracted layers to an ice core site in West Antarctica, showing the algorithm's ability to detect annual snow accumulation. Although not presented here, SAMPA's layer extracting utility could be used to investigate other scientific questions involving near-surface layering, including layer deformation from wind or layer compaction due to densification.

II. BACKGROUND

Tracking continuous isochronal internal layers over the ice sheets for hundreds to thousands of kilometers is difficult. Layers can naturally bifurcate or become less pronounced, while noncontiguous layers may appear for short distances related to a local anomaly not associated with the broad climatic pattern or

Manuscript received May 1, 2013; revised September 27, 2013, January 27, 2014, and March 7, 2014; accepted March 31, 2014. This work was supported by a collaborative grant between NASA's Airborne Science and Cryospheric Sciences Programs and the National Science Foundation Antarctic Glaciology Program.

V. P. Onana is with the Cryospheric Sciences Branch (Code 615), NASA Goddard Space Flight Center, Greenbelt, MD 20771 USA, and also with ADNET Systems Inc., Lanham, MD 20706 USA (e-mail: vincentdepaul.onana@nasa.gov).

L. S. Koenig and M. Studinger are with the Cryospheric Sciences Branch (Code 615), NASA Goddard Space Flight Center, Greenbelt, MD 20771 USA (e-mail: Lora.s.koenig@nasa.gov; michael.studinger@nasa.gov).

J. Ruth is with the Department of Physics, University of Maryland, College Park, MD 20740 USA (e-mail: jmruth@terpmail.umd.edu).

J. P. Harbeck is with the Cryospheric Sciences Branch (Code 615), NASA Goddard Space Flight Center, Greenbelt, MD 20771 USA; with ADNET Systems Inc., Lanham, MD 20706 USA, and also with the University of Alaska Fairbanks, Fairbanks, AK 99775 USA (e-mail: jeremy.p.harbeck@nasa.gov).

Color versions of one or more of the figures in this paper are available online at <http://ieeexplore.ieee.org>.

Digital Object Identifier 10.1109/TGRS.2014.2318208

event. Although difficult to extract, many approaches have been used to trace and track internal layers or ice surface and internal layers from radar echograms. Many studies have manually digitized layers (e.g., [7], [22], and [23]). This approach becomes prohibitively slow for long (thousands of kilometers) profile distances. The authors in [24]–[26] all used an interactive semiautomated means to insure accuracy and retrieve layers where discontinuities may occur. In [27], a method for the detection of near-surface Martian ice layers in orbital radar data was proposed. The method applies a series of filtering: first, a low-pass Gaussian filter enhances layers; next, a high-pass filter normalizes areas with high reflectivity with areas of low reflectivity. The authors then used a filter matched to the shape of the ice layers. The final layer detection is achieved by applying a threshold and morphological processing. Considering our high-resolution data set approximates 4.5-cm vertical resolution \times 20-cm along-track resolution, filtering steps combined with morphological processing are prohibited. Sime *et al.* [28] developed a fully automated processing method for picking internal layers and bed reflections using depth-sounding radar data. While the proposed method is useful for applications using depth-sounding radars, the resolution of the resulting extracted layers makes the application to high-resolution near-surface radars difficult. Specifically, the noise reduction step in the algorithm in [28] uses a horizontal and vertical moving average that degrades the original echograms' horizontal and vertical resolutions, resulting in thicker extracted layers. A major challenge when using conventional edge detection processes is the location of the resulting edges (e.g., [29]). Commonly, the resulting edges' location is fuzzy, which is an issue for applications trying to detect closely spaced annual layering. Very recently, Ferro and Bruzzone [30] have developed an automatic internal layer extraction method from radar sounder data sets. Their method uses several steps to carry the final layer extraction. In one particular step to highlight layer features before extracting them, the original resolution of the image is lost and, therefore, the subsequent layer extraction location. This method lacks a regularization step; therefore, some extracted layer segments are not connected and, thus, their trackability making it less than ideal for our ice-sheet application.

Continuous layers in near-surface radars, ranging from high to ultrahigh frequencies, have been shown in numerous studies to track isochronal layers over the ice sheets. The authors in [7] and [31] first showed that shallow 400-MHz radar data, which were gathered over the West Antarctic Ice Sheet (WAIS), contained isochronal layers with datable accuracy to ice cores of less than one year. In addition to high-/very high-frequency radars, ultra-/super-high-frequency (2–20 GHz), FMCW radars have been shown to map stratigraphic layers over ice sheets and ice caps at nearly annual rates (e.g., [32]–[34]). Additionally, Hawley *et al.* [35] first showed that an airborne radar at 13.2 GHz (Ku-band) could determine annual layers in the dry-snow zone of the Greenland ice sheet when compared to annual density peaks. Radar-echo-sounding layers in the near surface arise from a natural seasonal change in snow density on an annual cycle. These studies prove the utility of near-surface radars for measuring accumulation, but all used manual time-consuming methods for picking isochronal layers. The

approach presented in our study to track and trace surface and internal layers from radar echograms is based on the Radon transform (RT) computed from the original vertical and horizontal resolutions of the echogram, thus preserving the high-resolution image of the firn microstructure. The advantage of using the RT is that the transformation is rooted from a summation along layer features and it has the capability of carrying linear feature detection in a noisy surrounding with high location accuracy of the linear feature pixels, e.g., [36]. Unlike edge detection approaches that measure contrast between linear features and their surroundings, the RT maps linear features into a transformed domain, where thresholds are set for the peak's amplitude and width detection. Our method detects segmented-layer features over small blocks, assuming that, over a short-enough distance, a curved layer feature may be approximated with a line segment, and thus validating the use of the RT. We have organized the remaining article as follows. Section III presents the RT applied to firn layer detection; the probability density function (PDF) of peaks in the RT domain is also analyzed. The different steps of the SAMPA algorithm are provided in Section IV. Results, analysis, and an example of application of SAMPA's outputs are given in Section V. Finally, Section VI summarizes the SAMPA algorithm.

III. RT APPLIED TO FIRN LAYER DETECTION

Radar-sounded isochronous layers within the ice sheets resemble linear features carrying a variety of characteristics, including contrast inhomogeneity, discontinuity, natural bifurcation, and speckle noise. A variety of approaches for extracting imaged linear features have been proposed. The Canny–Derich detector [37] behaves well on natural images where high contrasts are measurable. Edges extracted using the Canny–Derich detector, however, suffer from a lack of location accuracy in certain scenarios (e.g., [29]). The ratio of local means has proven efficiency for amplitude radar imagery (e.g., [38]) and its applications, such as road detection (e.g., [39]). The RT (e.g., [40]) and its localized form (e.g., [41]) have been used for lines or line segment extraction in synthetic aperture radar images of rainforest areas (e.g., [36]). The summation inherent from the RT along linear features overcomes speckle effects in the resulting RT domain, where the detection of peaks is operated. While the conventional RT performs line detection even in noisy linear features, it cannot detect in the case of curved linear features naturally occurring within the isochronal ice-sheet layers. Parabolic and hyperbolic RTs have been used for certain specific applications (e.g., interpolation of seismic data [42], [43]), but do not replicate curved lines. Isochronous firn layers from ice sheets are randomly and continuously bending linear features, which are not ideal for a conventional RT.

Here, to take advantage of properties of the conventional RT for layer detection, such as the ability to carry linear feature detection in a noisy image and the extraction of segmented linear features, we first process curved features within small enough blocks to be considered straight, and second, we perform integrations of curved features by summations using a short integration length. Thus, we compute the forward RT within the corresponding blocks, and the resulting RT domain is marked

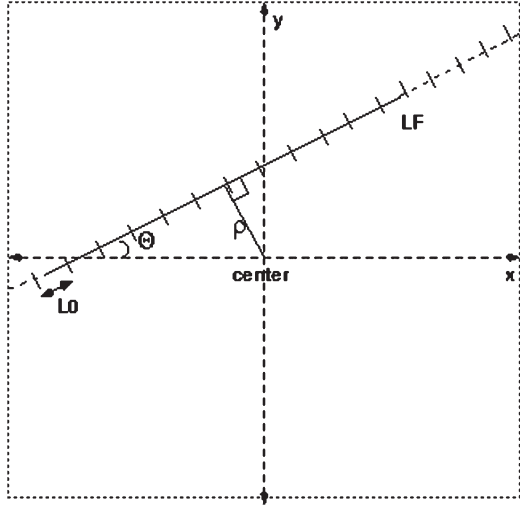


Fig. 1. Synopsis of a line feature (LF) in the echogram space represented with (ρ, θ, l) coordinates. The parameter l in (2) and (3) corresponds to the integration length $L0$ (shown in the figure) along the linear feature. ρ and θ are referenced from the center of the image. Elementary summations $s_i = \sum_{n=1}^{L0} p_n$ are computed over $L0$, and point sums in the DRT domain correspond to $N \cdot s_i$, where N is the number of elementary summations performed over $L0$ along the LF.

by dark or bright spots, which correspond to dark or bright segmented-layer features representing the curved features. Spot peaks can be more easily detected in the transformed domain than the original curved features in the radar echogram space. The back projection of the peaks from the transformed domain allows the extraction of segmented-layer features.

A. Mapping Multiple Firn Layers Into the RT Domain

Radar echograms of ice sheets are distinguishable by strong radar signal returns from interfaces caused by annual density changes. The echograms image these annual layers. The use of the RT maps these layer features into bright spots in the RT domain. Thus, the RT domain is made by point sums. Bright spots in the RT domain are detected using the peak's amplitude and width threshold parameters. That property of the RT makes it an efficient tool to highlight either dark or bright linear features even in a noisy and discontinuous surrounding.

1) *Forward RT (RT)*: The continuous RT $\mathcal{R}_c(\rho, \theta)$ of a 2-D lattice $I(x, y)$ with a compact support including the origin (the center of the lattice) is defined by [44]

$$\mathcal{R}_c(\rho, \theta) = \int_{-\infty}^{\infty} \int_{-\infty}^{\infty} I(x, y) \delta(x \cos \theta + y \sin \theta - \rho) dx dy \quad (1)$$

where (x, y) corresponds to a given Cartesian position within the lattice space, $\rho \in (-\infty, \infty)$ is the distance from the lattice center to the line feature, $\theta \in [0, \pi)$ is the angle between the line feature and the horizontal axis (see Fig. 1 for illustration), and δ is the Dirac distribution that converts the 2-D integral to the line integral along $x \cos \theta + y \sin \theta = \rho$. Hence, the RT is a set of projections along the angular directions θ of all potential line features from the distance ρ to the center of the lattice.

We consider that a point (x, y) of a given line feature making an angle θ with the x -axis is specified by the following three

real parameters: (l, ρ, θ) , where $l \in (-\infty, \infty)$ is a parameter along the line feature to integrate over it. Thus, the aforementioned parameterization implies that, for a fixed direction θ , the Cartesian coordinates (x, y) can be expressed in terms of local coordinates (l, ρ) on the line feature by

$$\begin{cases} x = \rho \cos \theta - l \sin \theta \\ y = \rho \sin \theta + l \cos \theta \end{cases} \quad (2)$$

such that (1) can be rewritten after combining with (2) as

$$\mathcal{R}_c(\rho, \theta) = \int_{-\infty}^{\infty} I(\rho \cos \theta - l \sin \theta, \rho \sin \theta + l \cos \theta) dl \quad (3)$$

where dl denotes the line integral along the line feature $x \cos \theta + y \sin \theta = \rho$.

Practical applications of the continuous RT deal with discrete domains such as images or echograms. Thus, we can write the discrete RT (DRT) $\mathcal{R}_d(\rho, \theta)$ from (3) as

$$\mathcal{R}_d(\rho, \theta) = \sum_{l=-\infty}^{\infty} I(\rho \cos \theta - l \sin \theta, \rho \sin \theta + l \cos \theta) \quad (4)$$

where the discretization step is considered to be one unit.

2) Bright or Dark Spot Peak Detection in the DRT Domain:

Fig. 2(a) and (b) depict a piece of an original echogram and the resulting DRT domain, respectively. Segmented-layer features in Fig. 2(a) correspond to peaks in the transformed domain in Fig. 2(b). The use of thresholds allows the detection of peaks' amplitude and width, as shown in Fig. 2(c). Correspondingly, if a linear feature in the echogram domain is bright or dark, then the resulting spot in the DRT domain will be bright or dark and will represent a maximum or a minimum point sum value s_i . Assuming that all point sums s_i in the DRT domain are independent and identically distributed (supposing that the length of integration $l = L0$ is small enough, i.e., $L0 \approx 1$ m for relatively flat layers, for our application), the PDF $\mathcal{H}(m)$ of detecting a peak in the DRT domain (i.e., a segmented layer within blocks), if it exists, is given by [45]

$$\mathcal{H}(m) = \begin{cases} N_{\text{DRT}} h(m) \left(\int_0^{\infty} h(m) dm \right)^{N_{\text{DRT}}-1}, & \text{case of peak (maximum) values} \\ N_{\text{DRT}} h(m) \left(1 - \int_0^{\infty} h(m) dm \right)^{N_{\text{DRT}}-1}, & \text{case of bottom (minimum) values} \end{cases} \quad (5)$$

where h is the PDF of the distribution of the DRT domain, and N_{DRT} is the number of point sums in the DRT domain.

The knowledge of the theoretical PDF of h is useful to analyze the behavior of the peak detection in the RT domain. Here, first, we have investigated the clutter, i.e., radar signal echo statistics modeling of the amplitude of Ku-band radar data of ice sheets. The goal was to derive a suitable PDF. The statistics modeling of the radar clutter distribution is important for algorithmic performance prediction, such as target detection and false-alarm probabilities [38], [39], [46]–[48]. Additionally, these statistics may be useful for Ku-band radar raw data processing consistency. To complete our investigation, we performed an analysis looking for the best theoretical fitted

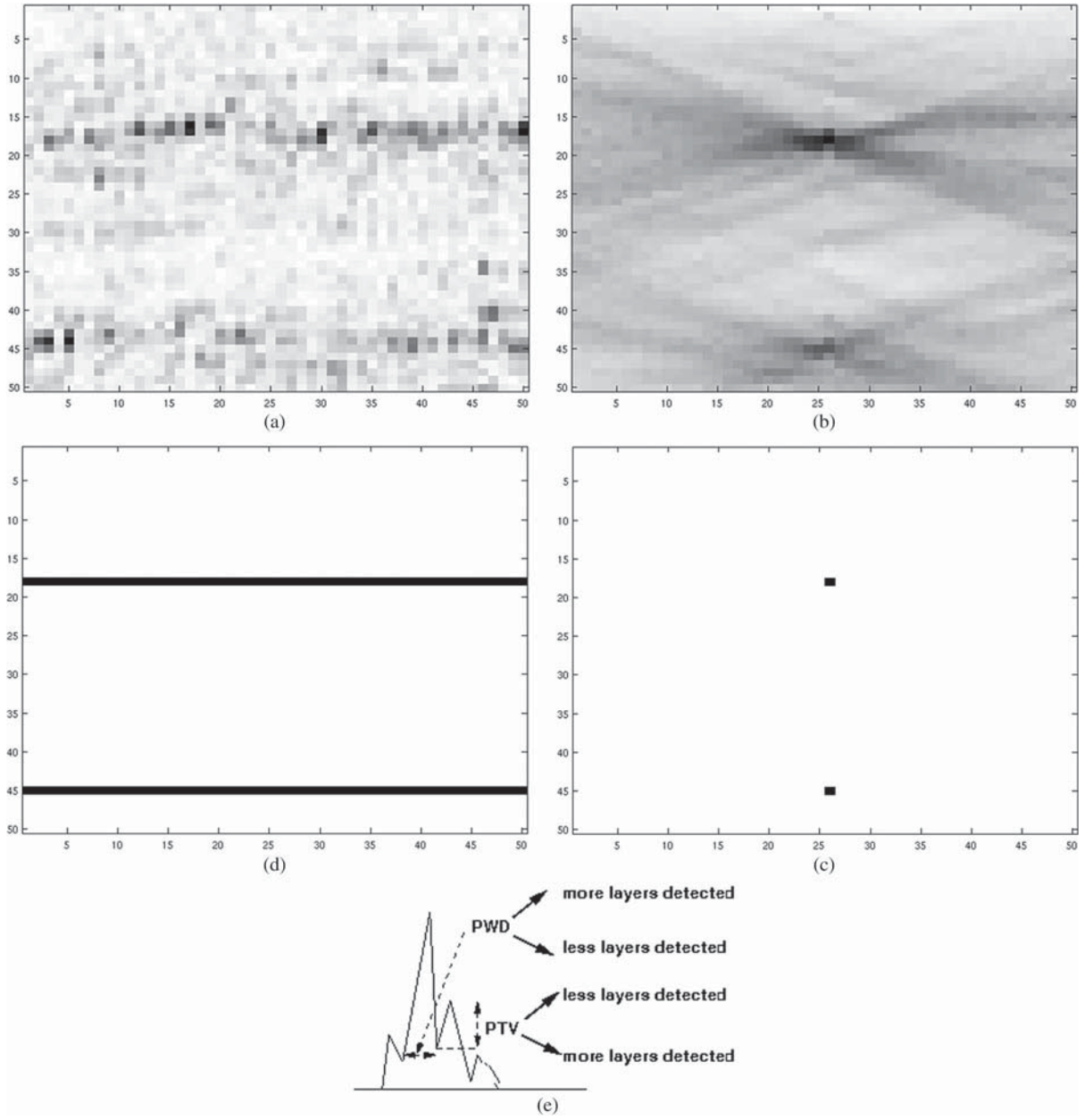


Fig. 2. Line feature extraction using the DRT. (a) Piece of an original echogram exhibiting two line features corresponding to two firm layers hardly visible. We note discontinuous behavior and roughness of line features. (b) Resulting DRT domain. We note two main peaks, i.e., two point sums corresponding to the two line features. (c) Resulting threshold output of (b). (d) Result after the application of the backward DRT of (c). Here, $l = L0 \approx 1$ m (5 pixels) for relatively flat layers, $PTV = 0.1$, $PWD = 4$, and $\theta \in [-\pi/5, \pi/5]$. (e) Illustration of a vertical profile of PWD and PTV parameters for peak detection in the DRT domain. The greater the value of PWD, the more layers are detected; the smaller the value of PTV, the more layers are detected. (b) and (c) are in $[x\text{-axis} = \theta\text{-axis and } y\text{-axis} = \rho\text{-axis}]$, whereas (a) and (d) are in the original image reference. ρ and θ parameters were sampled to the original image sizes in (a).

model of the clutter Ku-band radar amplitude distribution of ice sheets. We compare the empirical PDF of Ku-band radar amplitude data with the following conventional and theoretical unimodal distributions and their associated PDF for a given target (i.e., a pixel value $p_n \geq 0$): log-normal, Weibull, gamma, and K distributions. We then used the conventional Kolmogorov–Smirnov test (KS-test) [49] and the Kullback–Leibler [50] distance (KLD) to carry out the goodness-of-fit theoretical distribution for the amplitude of Ku-band radar echograms. As a result, both the KS-test statistics and the KLD have substantiated that the theoretical log-normal PDF is the best fit for the amplitude of Ku-band radar echograms of ice sheets.

Using a different data set, Ferro and Bruzzone [48] similarly studied the statistical distributions of radar sounder signals of ice sheets of the Shallow Radar (SHARAD) onboard the Mars Reconnaissance Orbiter of NASA. Their analysis substantiated that the K distribution is suitable to model strong and weak layers. Here, the Ku-band radar data follow the theoretical log-normal distribution $\mathcal{L}(p > 0 | \mu_l, \sigma_l) = (1/p\sigma_l\sqrt{2\pi}) \exp(-((\ln(p) - \mu_l)^2/2\sigma_l^2))$, where μ_l and σ_l represent the mean and the standard deviation, respectively; therefore, a point sum s_i of the DRT domain follows the sum of log-normal distributions. Finding a close analytical expression of the sum of log-normal distributions, however, is an open problem; there is

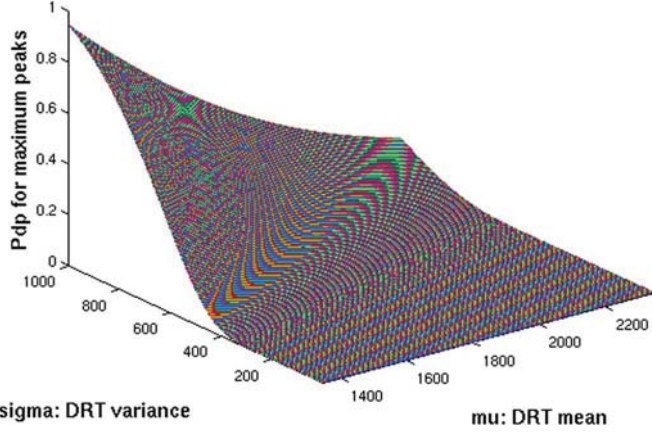


Fig. 3. Theoretical probability of detecting peaks Pdp in the DRT domain versus the mean μ_l (μ) and the standard deviation σ_l (σ); with $N=10$ being the number of elementary summations over the length of integration $L_0=5$, $N_{DRT}=50 \times 50$ the number of point sums in the DRT domain. Note that point sum values in the DRT domain are on the order of magnitude 10^9 ; hence, $[DRT_{\max 1}=10^9, DRT_{\max 2}=10^{10}]$ is the range of point sums containing peaks in the DRT domain. On a given segmented layer within a block, the Pdp increases as σ_l increases, and $Pdp > 0.8$, for $\sigma_l = 10^3$, for the range $[DRT_{\max 1}, DRT_{\max 2}]$ used for the simulation. This analysis substantiated that high signal return echoes (i.e., with a high variance of segmented-layer points) contribute to a high detectability of peaks in the DRT domain.

no exact analytical expression. Using the following assumption: *Within a block, pixels belonging to a given segmented layer have close intensity values p_0 ; therefore, a point sum in the DRT domain can be approximated by $s_i = N \sum_{n=1}^{L_0} p_n \approx N \cdot L_0 \cdot p_0$.* It becomes much easier to assess the PDF h of a point sum s_i (see more details in Appendix I) as follows:

$$h_{\{s_i, N, L_0, \mu_l, \sigma_l\}}(p) = \frac{1}{N \cdot L_0} \mathcal{L}\left(\frac{p}{N \cdot L_0} > 0 | \mu_l, \sigma_l\right) \\ = \frac{1}{p \sigma_l \sqrt{2\pi}} \exp\left(-\frac{(\ln(\frac{p}{N \cdot L_0}) - \mu_l)^2}{2\sigma_l^2}\right) \quad (6)$$

where N is the number of elementary summations $\sum_{n=1}^{L_0} p_n$ along a linear feature (see Fig. 1).

From (5), the probability of detecting peaks Pdp , in the DRT domain, is then given by

$$Pdp = \int_{DRT_{\max 1}}^{DRT_{\max 2}} \mathcal{H}(m) dm \\ = \frac{N_{DRT}}{2} \left[\operatorname{erf}\left(\frac{\ln(\frac{DRT_{\max 2}}{N \cdot L_0}) - (\mu_l + \sigma_l^2)}{\sigma_l \sqrt{2}} + \frac{\sigma_l}{\sqrt{2}}\right) \right. \\ \left. - \operatorname{erf}\left(\frac{\ln(\frac{DRT_{\max 1}}{N \cdot L_0}) - (\mu_l + \sigma_l^2)}{\sigma_l \sqrt{2}} + \frac{\sigma_l}{\sqrt{2}}\right) \right] \quad (7)$$

where N_{DRT} is the number of points [i.e., point sum s_i] in the DRT domain, $\operatorname{erf}(x)$ represents the error function defined by $\operatorname{erf}(x) = (2/\sqrt{\pi}) \int_0^x \exp(-t^2) dt$, and $[DRT_{\max 1}, DRT_{\max 2}]$ is the range of integration containing peak values in the DRT domain. Fig. 3 depicts the theoretical probability of detecting peaks Pdp in the DRT domain, for $N_{DRT} = 50 \times$

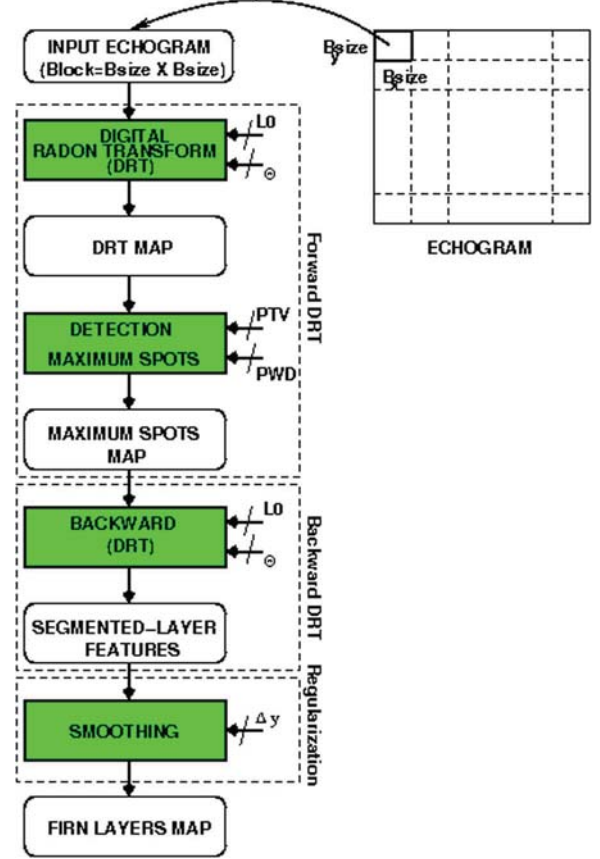


Fig. 4. Description of SAMPA for ice-sheet radar echogram. Control parameters are presented as follows: $l = L_0$, the length of integration along line features, typically $L_0 \leq 1$ m (5 pixels) for relatively flat layers; PTV, the peak's amplitude threshold value, which represents the height of peaks to be detected, typically $PTV \in [0.1, 0.5]$; PWD, the peak's width to be detected, corresponds to the width of peaks to be detected, typically $PWD \in [4, 20]$. $B_xsize, B_y size$, the block size dimensions, typically $B_xsize \times B_y size \leq 2.25$ m \times 20 m (50×50 pixels); θ , the angular orientation range, typically $\theta \in [-\pi/2, \pi/2]$; and $\Delta y \approx 22.5$ cm (5 pixels) vertical distance within which layer points are considered to belong to the same layer feature.

50 point sums, $N = 10$, $L_0 = 5$, and the range $[DRT_{\max 1} = 10^9, DRT_{\max 2} = 10^{10}]$. On a given segmented layer within a block, the Pdp increases as σ_l increases, and $Pdp > 0.8$, for $\sigma_l = 10^3$, for the range of point sums used for the simulation. This analysis substantiated that high signal return echoes (i.e., with high variance of segmented-layer points) contribute to a high detectability of peaks in the DRT domain, thus supporting the efficiency of using the RT to detect firm layer features from echograms.

B. Firm Multilayer Feature Extraction From the DRT Domain

After the detection of peaks in the DRT domain, due to the reversibility of the RT, a backward DRT is computed to get back only the expected segmented-layer features in the original space. There are a number of backward RT formulas. The following has been derived by [44]:

$$I(x, y) = -\frac{1}{2\pi^2} \int_0^\pi \int_0^\infty \frac{(\partial \mathcal{R}_c / \partial \rho)(\rho, \theta)}{\rho - (y \cos \theta + x \sin \theta)} d\rho d\theta. \quad (8)$$

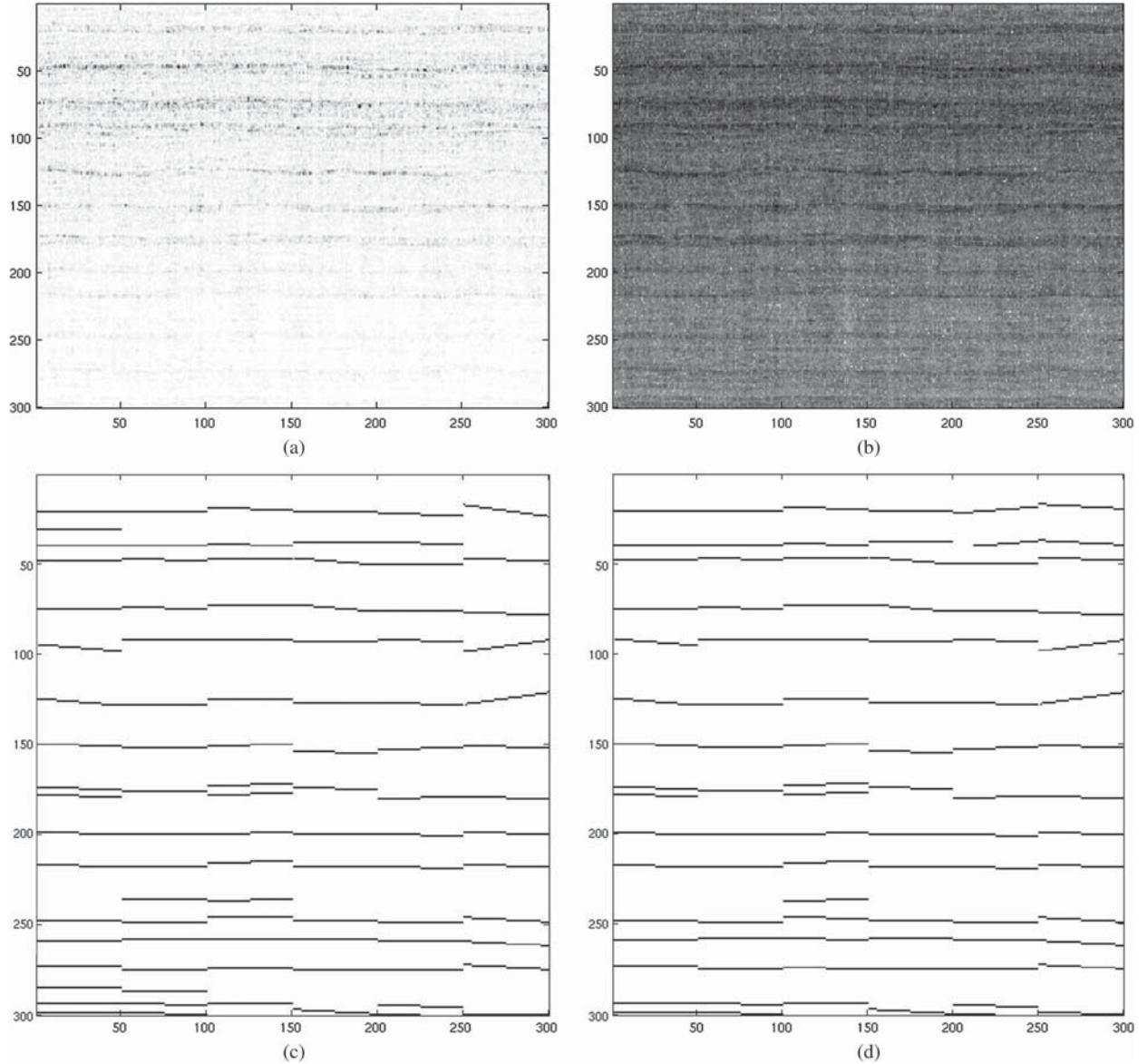


Fig. 5. Effect of variation of the length of integration $l = L_0$ on extracted segmented-layers, $B_x \text{ size} \times B_y \text{ size} \approx 10 \text{ m} \times 2.25 \text{ m}$ (50×50 pixels), $\text{PTV} = 0.3$, $\text{PWD} = 20$, and $\theta \in [-\pi/5, \pi/5]$, [x -axis = θ -axis and y -axis = ρ -axis]. (a) Piece of an original amplitude of echogram: we note stronger return layers on the top and lower return layers on the bottom. (b) Log amplitude of echogram in (a). Note that the log amplitude better highlights layers comparing with (a) and was used, instead, to lower point sum values in the RT domain. (c) Extracted segmented-layers using $L_0 \approx 1 \text{ m}$ (5 pixels) for relatively flat layers and (d) extracted segmented-layers using $L_0 \approx 10 \text{ m}$ (50 pixels); as $l = L_0$ increases, we note three phenomena: smoothing of some layers, filling of some segmented layers, and depletion of some segmented layers. Smoothing and depletion cannot be corrected, whereas filling can be partially corrected using a regularization step.

Conventional backward RT formulas are used to get the exact original distribution of $I(x, y)$. Here, when focusing on peaks representing segmented-layer features in the DRT domain, after applying thresholds, we leave with few point sums [i.e., only peaks; see Fig. 2(c)] from which we would like to extract the original corresponding segmented-layer features. Therefore, the use of (8) is processing time consuming, and back projections to the original space suffice to extract the expected segmented-layer features using (4).

Fig. 2(d) depicts the result of the application of the DRT, which is followed by the back projection of the two peaks in Fig. 2(c) to the original space of Fig. 2(a), allowing to get back the two corresponding segmented-layer features.

IV. SAMPA FOR ICE-SHEET RADAR ECHOGRAMS

Fig. 4 presents the different steps used in the SAMPA algorithm to track and trace isochronous firm layers from radar echograms. The input echogram is divided into blocks of same size, for instance, $B_x \text{ size} \times B_y \text{ size}$, and each block is processed individually through the steps described in Fig. 4. Once each block is processed, the resulting extracted segmented-layers are projected back to the original block space. This approach was based on the assumption that a short-enough line segment, to even a curved line, can be considered straight and was also adopted to smooth the final layer pick. Note that the log amplitude of the imaged echogram better highlights layers, as shown in Fig. 5(b) compared to Fig. 5(a); moreover, the

DRT is a cumulative summation process. Applying the DRT on a log echogram (log amplitude) instead allows avoiding dealing with very large values (order of magnitude $> 10^9$) in the DRT domain. Thus, the log of the echogram is processed by following the steps.

A. Step #1: Computation of the DRT

The computation of the DRT requires specific parameters to be set. These parameters will vary based on the specific application and the quality of the radar echogram. The parameters and their function in the SAMPA algorithm are described in the following. B_xsize and B_ysize represent the optimal horizontal and vertical dimensions of a block size, respectively; $L0$ represents the optimal length of integration along the line features; and θ represents the angular orientation range. The outputs of this step are DRT maps [see illustrations in Figs. 2(b) and 6(a)]. For the Ku-band radar echograms processed here, the optimal ranges for the three input parameters are the following.

- The block size $B_xsize \times B_ysize$ is chosen within $\approx [10 \text{ m} \times 2.25 \text{ m}, 20 \text{ m} \times 4.5 \text{ m}]$; using a much larger block size will result in smoothing the firm layers' undulations into straight line-segments. Smaller block sizes will result in a long processing time and may increase false detections in the scenario where few radar echoes are available within blocks.
- The choice of the integration length $L0$ is also important. Smaller values of $L0$ lead to fine integration along segmented-layer features for the computation of the DRT and the backward DRT, whereas greater values of $L0$ lead to rough integrations. Smaller values of integration length, moreover, lead to a good reconstruction of the layer features, as shown in Fig. 5(c) and (d). A length of integration $L0 \approx 1 \text{ m}$ for relatively flat layers is optimal for our application for the computation of DRT and the backward DRT of input echograms' blocks. Increasing $L0$ leads to the smoothing of some final picked layers, over filling of other segmented layers (i.e., possibility of connecting different spaced segmented-layer features by integration), and depletion of some segmented-layer features (i.e., case of presence of few layer echoes that can be integrated with non layer echoes). Smoothing and depletion cannot be corrected in any other step of the algorithm, but correcting the segmented layers is partially corrected in the regularization step.
- Last is the choice of θ , which is the angular orientation range. θ depends on the layers' local slope. The flatter the layers, the smaller the angular orientation range. Imaged layers from echograms of our data set are relatively flat; the angular orientation range of $[-\pi/5, \pi/5]$ works well. Using a much bigger range comparing to the layers' local slope, however, will increase the DRT time processing, but may not improve the overall performances.

B. Step #2: Peak Detection in the DRT Domain

In Section III-A2, we demonstrated that high signal return echoes contribute to a high detectability of peaks in the DRT

domain. High signal return echoes correspond to layer points in the echogram and peaks in the DRT domain. Therefore, we have high confidence that detecting peaks in the DRT domain leads to detecting corresponding layers in the echogram. Moreover, setting thresholds while detecting peaks in the DRT domain corresponds to fixing a certain level of probability of detection of segmented layers. Inputs for peak detection require threshold values to determine which maxima in the DRT domain should be picked as segmented layers. The inputs **PTV**, i.e., the peak's amplitude threshold value, and **PWD**, i.e., the peak's width to detect in the DRT domain, are needed for the detection of peaks, as illustrated in Fig. 2(e). The PTV describes the heights of the peaks, and the PWD describes the widths of the peaks. The outputs of this step are the peaks' maps, as illustrated in Fig. 6(b) and (c). Greater values of PWD allows the detection of more peaks, whereas smaller values of PWD permits the detection of fewer peaks, as shown in Fig. 2(e). Between the two threshold parameters PTV and PWD, the latter may affect the result if not cautiously tuned. For our application using near-surface radar echograms with relatively flat layers, the following range is chosen by tuning the algorithm to most closely pick the visible layers in the echogram, i.e., $PWD \geq 4$. Moreover, the parameter PTV represents the percentage of the peak value to consider for the extraction of layer features from the DRT domain. As PTV increases, the number of peaks detected in the DRT domain decreases, leading to the extraction of fewer layers. Smaller values of PTV not only allow the extraction of more layers but also tend to increase false detections. Layers' signal return echoes are inhomogeneous, i.e., layer feature echoes do not have the same peak's amplitude across the echogram. Thus, that creates an uncertainty while detecting peaks in the DRT domain and by, while extracting the corresponding segmented layers. That uncertainty leads to false detection. Moreover, the existence of uncertainty implies that the false detection rate cannot be null. A compromise has to be made based on the end-user goals to minimize false detections. The final results presented in this paper used $PTV \in [0.1, 0.5]$. Fig. 6(d) ($PWD = 20$ and $PTV = 0.1$) and Fig. 6(e) ($PWD = 4$ and $PTV = 0.1$) depict the profile from the column where the peaks are located in Fig. 6(b) and (c), respectively, highlighting the effect of the variation of the two parameters.

C. Step #3: Segmented-Layer Feature Extraction

The detection of peaks from the DRT domain produces the segmented-layer features to be extracted. Thus, back projections are computed for each peak leading to the extraction of segmented-layer features in the original space. The following inputs are set in this step: the block size dimensions B_xsize and B_ysize ; the length of integration $L0$; and the angular orientation range θ used in Step #1. The output of this step is the map of segmented-layer features, as shown in Fig. 7(b).

D. Step #4: Regularization of Segmented-Layer Features

Fig. 7(a) depicts an original Ku-band radar echogram, and the resulting segmented-layer features are shown in Fig. 7(b). Some extracted segmented-layer features after applying the backward

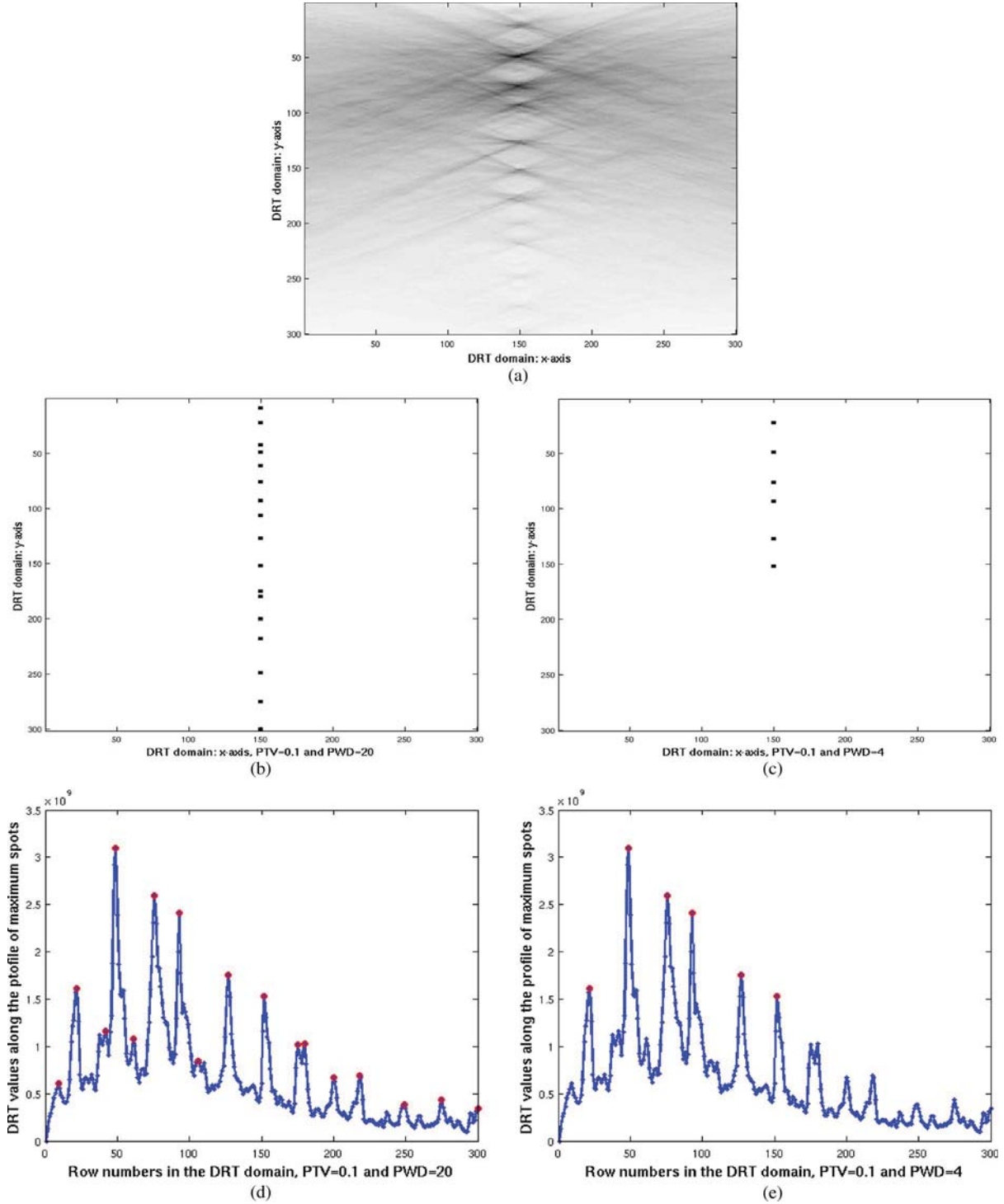


Fig. 6. Effect of variation of PWD in the DRT domain for fixed PTV, $L_0 \approx 1$ m (5 pixels) for relatively flat layers, and $\theta \in [-\pi/5, \pi/5]$, [x -axis = θ -axis and y -axis = ρ -axis]: (a) DRT domain computed from a piece of an original amplitude echogram in Fig. 5(a). (b) PTV = 0.1 [i.e., $\geq 10\%$ of the maximum value in the DRT domain in (a)] and PWD = 20. (c) PTV = 0.1 and PWD = 4. (d) Profile of the column where the DRT maximum values are detected, PWD = 20 and PTV = 0.1. (e) Profile for PWD = 4 and PTV = 0.1. For a fixed PTV, as PWD increases, the number of peak values detected in the DRT domain increases leading to the detection of more layers [note the number of bullet peaks in (d)]. Smaller values of PWD allow the detection of fewer layers [see in (c)].

DRT are noisy and disjunct, as shown in Fig. 7(b). That is due to detected nonphysical layers and to partly contrasted layers mostly resulting to anomalies. Visible firm layers on echograms fit into different categories, including Contrasted/Less Contrasted Layers Across the Echogram (CLAE/LCLAE) and Partly Contrasted/Less Contrasted Layers Across the Echogram (PCLAE/PLCLAE). We do not consider compressed layers

here, which may be hard visible. In some scientific applications such as accumulation estimation, the trackability of most extracted layer features is required. Therefore, underlying segmented layers of layer features that have lost parts due to anomalies need to be connected. Thus, resulting extracted segmented-layers are treated based on their trackability across the echogram as follows: CLAE/LCLAE and PCLAE/PLCLAE

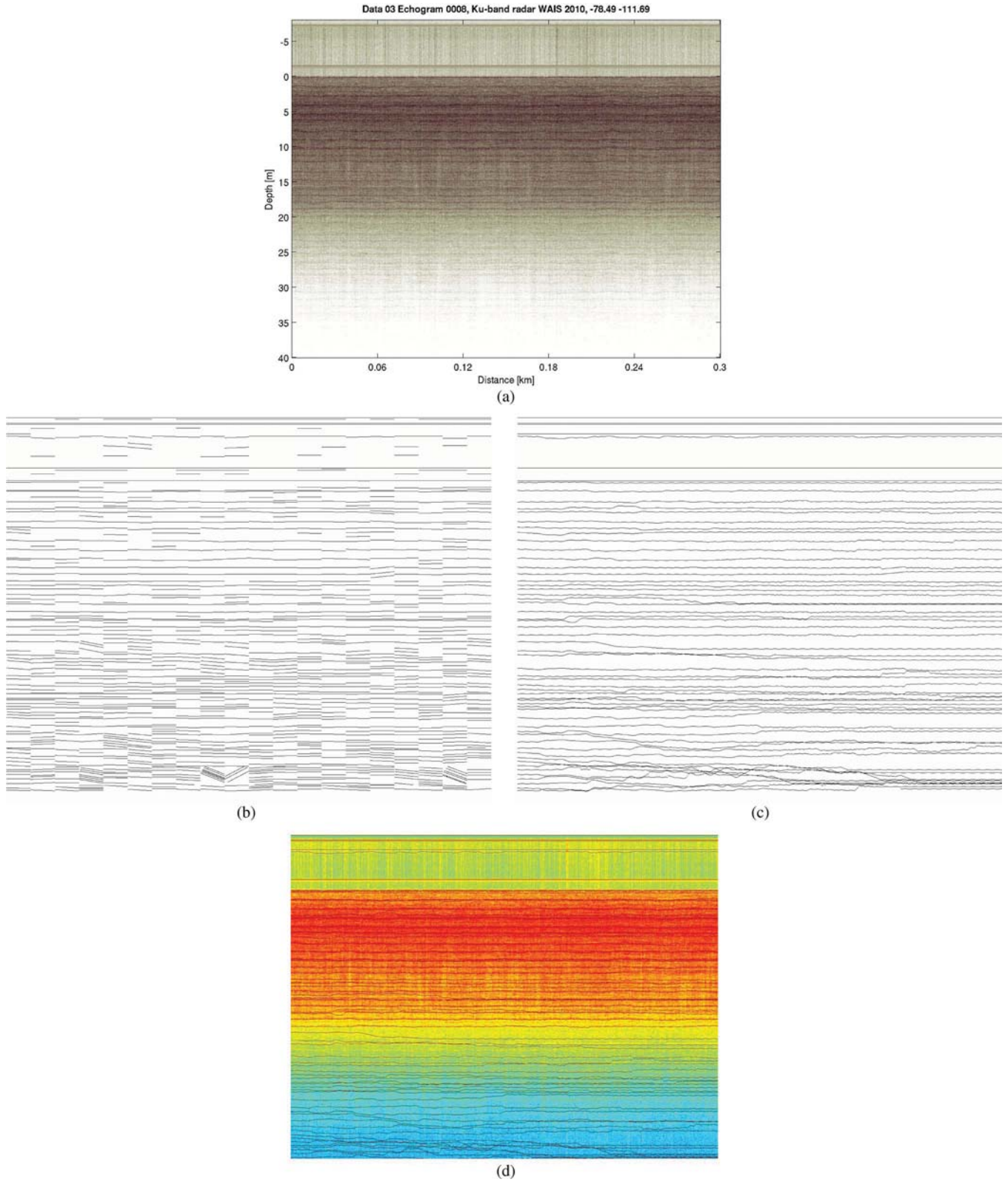


Fig. 7. Layer tracking results. (a) Original Ku-band radar data 03 echogram 0008. (b) Extracted segmented-layers. (c) Final result after the smoothing procedure. (d) Final result overlapping the original echogram in (a). B_x size \times B_y size $\approx 10 \text{ m} \times 2.25 \text{ m}$ (50×50 pixels); $L_0 \approx 1 \text{ m}$ (5 pixels) for relatively flat layers; $PTV = 0.1$; $PWD = 20$; and $\theta \in [-\pi/5, \pi/5]$. Upper layers are better extracted than lower layers due to lower signal returns in deeper layers. Thus, the reliability of the extraction of deeper layers decreases along with their trackability.

lying within less than half the long track of the echogram are ignored due to their lack of trackability across the echogram. CLAE/LCLAE and PCLAE/PLCLAE lying within more than

half the long track of the echogram are kept and then connected and smoothed. Hence, a regularization process that aims at connecting and smoothing extracted segmented-layers is necessary

TABLE I
ALL PARAMETERS USED ALONG WITH THEIR FUNCTIONS IN THE SAMPALGORITHM

Parameters	SAMPA Step set in	Functions
$B_x size, B_y size$	DRT and backward DRT	Block size: used in the computation of the forward and the backward DRT by block
$L0$	DRT and backward DRT	Length of integration: used in the computation of the forward and backward DRT
θ	DRT and backward DRT	Orientation angle range: used in the computation of the forward and backward DRT
PTV	Peak detection in DRT space	peak threshold value: sets the minimum amplitude for a peak to be considered
PWD	Peak detection in DRT space	peak's width to detect: sets a range of amplitude values within which peaks are considered
Δy	Smoothing process initialization	Vertical bins distance within to consider two segmented-lines belonging to the same layer

to achieve the final layer tracking. Extracted segmented-layers are then connected if they are vertically within Δy pixels and are indexed to be the same feature. Tests have conducted to choose $\Delta y \approx 22.5$ cm for echograms of our data set. The use of lesser values lowers the layer detection probability, whereas greater values tend to connect return signal echoes from different depth. The regularization step connects and smooths extracted layers, as depicted in Fig. 7(c). There are numerous smoothing algorithms. Here, we use a smoothing procedure based on the fully automated algorithm developed in [51]. The smoothing algorithm can work with evenly spaced data, deals with weighted data, can account for the occurrence of missing values, and self-carries the estimation of the smoothing parameter. The smoothing algorithm estimates the final smoothed layer from the extracted segmented-layers using an iterative scheme algorithm (see Appendix II for details). In practice, less than ten iterations are sufficient to get an acceptable smoothing result.

All parameters used by the SAMPAL algorithm and their functions are described in Table I. Although the DRT is a geometric integral, the resulting DRT domain carries radiometric information from the original echogram due to the existence of the inverse RT. Hence, the radiometry information is taken into account while detecting peaks in the DRT domain. However, peak detection in the DRT domain carries uncertainty inherent from the radiometric layer features' uncertainty of the original echogram, uncertainty that results to false or missing detection.

E. Step #5: Averaging of Layers' Picks Along Track

Once the picked vertical layers are established by SAMPAL, the picks are summed along the y -axis for some given distance along the x -axis, in our case ≈ 1 km along track. This results in a single layer depth pick across the specific x distance. SAMPAL uses the higher resolution radar data for all of the layer picking, but this final step reduces the resolution specifically for the final physical application. This averaging step could be turned on or off depending on the scientific application.

V. RESULTS AND ANALYSIS

A. Data Description

We tested the SAMPAL algorithm on two Ku-band radar echogram data sets, i.e., one airborne and one ground-based: The Ku-band Radar was built by the Center for Remote Sensing of Ice Sheets (CRISIS) at the University of Kansas

(<https://data.cresis.ku.edu/#KBRA>), and it has a typical sweep from 13 to 17 GHz. This radar images the near-surface firn to depths of over 20 m, in dry firn conditions. The technical specifications of the instrument are given in [52], and the data processing detailed is outlined at (<http://nsidc.org/data/docs/daac/icebridge/irkub1b/>). The primary purpose of this radar is high-precision surface elevation measurements over polar ice sheets, although the instrument can be also used to map annual layers with a high vertical resolution of ≈ 4.5 cm and along-track resolution of ≈ 20 cm. The radar illuminates individual spots, with a diameter size of ≈ 2 m, that are stacked to improve the along-track resolution. Hence, the echogram pixel size approximates $4.5 \text{ cm} \times 20 \text{ cm}$. The original data domain is the amplitude. To lower DRT domain values, the data are then converted into decibels before processing. Here, we use echograms collected during two different field campaigns that used the same Ku-band radar. SAMPAL was run on an airborne data set, i.e., the NASA's IceBridge Ku-Band Radar L1B Geolocated Radar Echo Strength Profiles data, collected during one flight over West Antarctica by the National Snow and Ice Data Center [53]. We also tested SAMPAL on a ground-based data set collected during the Satellite Era Accumulation Traverse (SEAT) in 2010 [54]. Here, we show only the results from the ground-based data, which are similar to the airborne results. The ground-based data were used because it has a higher along-track resolution of 20 cm versus 5.6 m for an airborne data set.

B. Results

The SAMPAL algorithm was applied to a radar echogram taken in West Antarctic. This region is known for relatively flat firn layers. The algorithm was run and the parameters trained. For our application using near-surface radar echograms with relatively flat layers, the following values were chosen by tuning the algorithm to closely pick the visible layers in the echogram: the block size $B_x size \times B_y size \approx 10 \text{ m} \times 2.25 \text{ m}$ (50×50 pixels); the integration length $L0 \approx 1 \text{ m}$ (5 pixels); the peak's width to detect $PWD = 20$; the peak's amplitude threshold value $PTV = 0.1$; the angular orientation range $\theta = [-\pi/5, \pi/5]$; and $\Delta y \approx 22.5 \text{ cm}$ (5 pixels vertically).

For the results reported in this paper, we discarded CLAE/LCLAE and PLCLAE lying within less than $< 200 \text{ m}$ of the echogram, due to their lack of trackability across wide. However, CLAE/LCLAE and PLCLAE lying within $\geq 200 \text{ m}$ of the echogram are retained for the regularization step. Fig. 7(c) depicts the final result of extracted layers from the

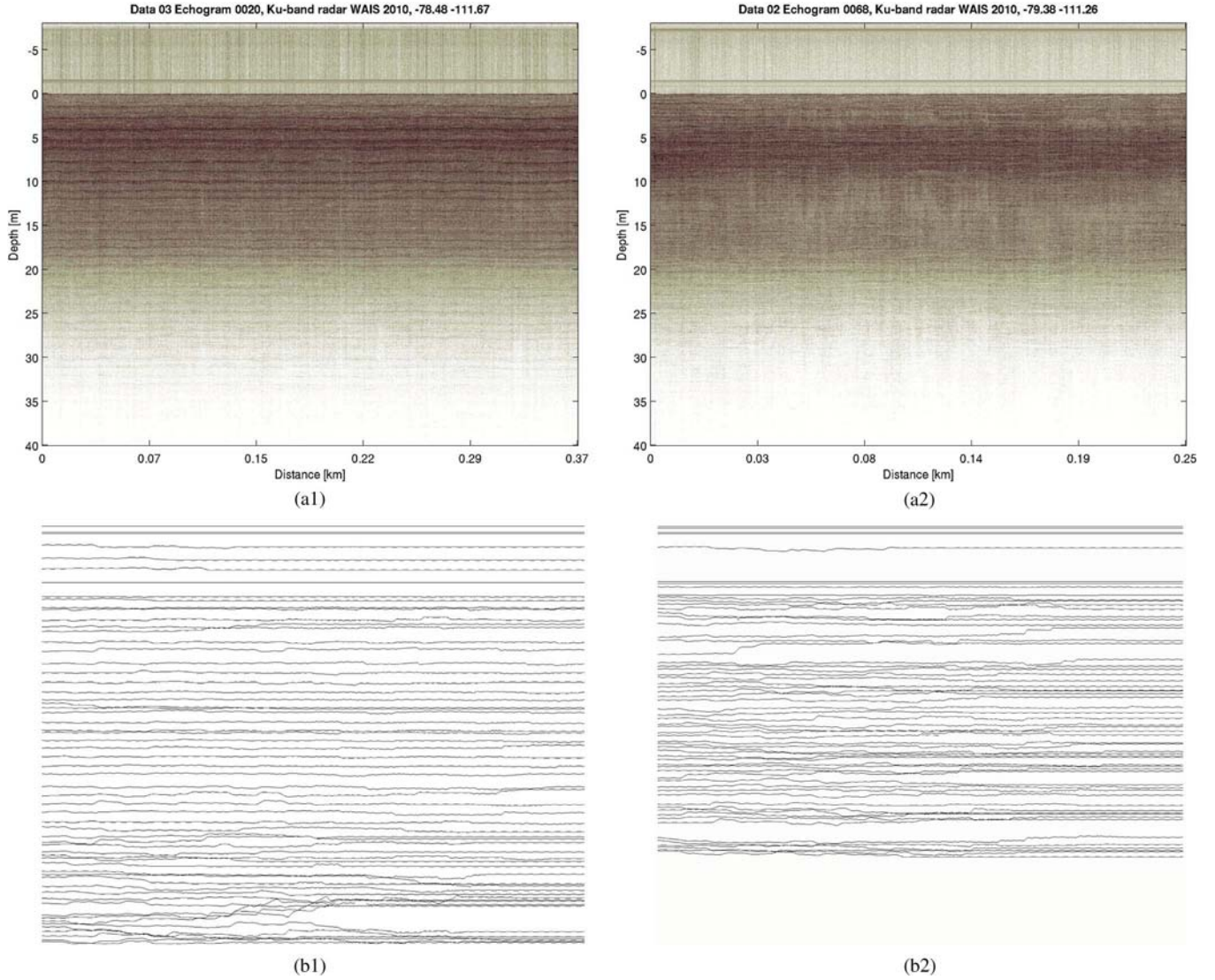


Fig. 8. Additional layer tracking results: (a1) original Ku-band radar data 03 echogram 0020; (a2) original Ku-band radar data 02 echogram 0068; (b1) final result data 03 echogram 0020 after the smoothing procedure of a1); (b2) final result data 02 echogram 0068 after the smoothing procedure of a2); $B_x \text{ size} \times B_y \text{ size} \approx 10 \text{ m} \times 2.25 \text{ m}$ (50×50 pixels), $l = L0 \approx 1 \text{ m}$ (5 pixels) for relatively flat layers, $PTV = 0.1$, $PWD = 20$, and $\theta \in [-\pi/5, \pi/5]$. Bottom layers in (a2) are much less pronounced, therefore, the resulting extraction in (b2).

TABLE II

SUMMARY OF ALL PARAMETER SETTINGS USED BY THE SAMPA ALGORITHM. RECOMMENDED RANGES AND VALUES WERE USED FOR RESULTS PRESENTED IN THE STUDY. $B_x \text{ size} \times B_y \text{ size}$: BLOCK SIZE'S DIMENSIONS, $L0$: INTEGRATION LENGTH, AND θ : ANGULAR ORIENTATION ARE USED TO COMPUTE FORWARD AND BACKWARD DRT. PTV: PEAK'S AMPLITUDE THRESHOLD VALUE, PWD: PEAK'S WIDTH TO DETECT, AND Δy : VERTICAL SHIFT WITHIN WHICH TWO SEGMENTED-LAYER FEATURES ARE CONSIDERED TO BELONG TO THE SAME LAYER ARE USED IN THE DETECTION STEP. HERE, $B_x \text{ size}$, $B_y \text{ size}$, $L0$ ARE EXPRESSED IN NUMBER OF PIXELS, AND A PIXEL'S DIMENSION $\approx 4.5 \text{ cm} \times 20 \text{ cm}$

	Forward DRT			Spot Peak detection			Backward DRT		
Parameters	$B_x \text{ size}, B_y \text{ size}$	$L0$	θ	PTV	PWD	Δy	$B_x \text{ size}, B_y \text{ size}$	$L0$	θ
Range	[50, 100]	[1, 5]	$[-\pi/2, \pi/2]$	[0.1 0.5]	[4, 100]	[5, 20]	[50, 100]	[1, 5]	$[-\pi/2, \pi/2]$
Value used	{50}	{5}	$[-\pi/5, \pi/5]$	{0.1}	{20}	{5}	{50}	{5}	$[-\pi/5, \pi/5]$

Ku-band radar echogram in Fig. 7(a) after the regularization step. Most picked layers are continuous and smoothed. There is no better way of assessing the localization accuracy of an extracted layer feature than lining it up above the original echogram. Hence, we superimposed extracted layers with the

original echogram in Fig. 7(d) for a visual check of location accuracy of picked layers. Additional layer extraction results are shown in Fig. 8(b1) and (b2). Table II summarizes all parameters and recommended ranges and their exact values set for the final results presented in this paper.

TABLE III

SAMPA LAYER TRACKING PERFORMANCE EVALUATION FROM THE ECHOGRAMS IN FIG. 7(a) AND FIG. 8(a1) AND (a2). THESE PERFORMANCES ARE INDICATIVE AND MAY LIGHTLY VARY BASED ON THE QUALITY OF THE ECHOGRAM. #X, X = PERFORMANCE NUMBER AND THE CORRESPONDING PERCENTAGE; #V, V = VISUALLY DETECTED LAYERS BY AN EXPERT; #G, G = GOOD DETECTED LAYERS, I.E., LAYERS THAT ARE VISUALLY DETECTED BY AN EXPERT AND ARE AUTOMATICALLY DETECTED BY SAMPA, INCLUDING PARTIALLY DETECTED LAYERS; #F, F = FALSE DETECTED LAYERS, I.E., LAYERS DETECTED BY SAMPA BUT ARE NOT VISUALLY DETECTED BY AN EXPERT; #M, M = MISSING DETECTED LAYERS, I.E., LAYERS THAT ARE VISUALLY DETECTED BY AN EXPERT BUT ARE NOT AUTOMATICALLY DETECTED BY SAMPA. COLUMNS LAYER SAMPA: GOOD AND LAYER SAMPA: FALSE REPRESENT TRACKING RATE AND FALSE DETECTION RATE RELATIVELY TO VISUALLY DETECTED LAYERS BY AN EXPERT, RESPECTIVELY. WE NOTE THAT SAMPA PROVIDES BETTER DETECTION RATE AND LOWER FALSE DETECTION PROBABILITY FOR UPPER LAYERS THAN FOR DEEPER LAYERS. GLOBAL PERFORMANCES ARE ALSO PROVIDED FOR EACH ECHOGRAM

UPPER Layer Tracking				LOWER Layer Tracking			
Data 03 Echogram 0008 - Global: V=60/60 (100%), G=82%,F=17%,M=18%							
Visual: #V	SAMPA: #G	SAMPA: #F	SAMPA: #M	Visual: #V	SAMPA: #G	SAMPA: #F	SAMPA: #M
30	30	4	0	30	19	6	11
#V/#V	#G/#V	#F/#V	#M/#V	#V/#V	#G/#V	#F/#V	#M/#V
30/30 (100%)	30/30 (100%)	4/30 (13.4%)	0/30 (0%)	30/30 (100%)	19/30 (63%)	6/30 (20%)	11/30 (37%)
Data 03 Echogram 0020 - Global: V=57/57 (100%), G=84%, F=17.5%, M=16%							
Visual: #V	SAMPA: #G	SAMPA: #F	SAMPA: #M	Visual: #V	SAMPA: #G	SAMPA: #F	SAMPA: #M
27	26	3	1	30	22	7	8
#V/#V	#G/#V	#F/#V	#M/#V	#V/#V	#G/#V	#F/#V	#M/#V
27/27 (100%)	26/27 (96%)	3/27 (11%)	1/27 (4%)	30/30 (100%)	22/30 (73%)	7/30 (23%)	8/30 (27%)
Data 02 Echogram 0068 - Global: V=60/60 (100%), G=87%, F=28%, M=13%							
Visual: #V	SAMPA: #G	SAMPA: #F	SAMPA: #M	Visual: #V	SAMPA: #G	SAMPA: #F	SAMPA: #M
39	34	12	5	21	18	5	3
#V/#V	#G/#V	#F/#V	#M/#V	#V/#V	#G/#V	#F/#V	#M/#V
39/39 (100%)	34/39 (87%)	12/39 (31%)	5/39 (13%)	21/21 (100%)	18/21 (86%)	5/21 (24%)	3/21 (14%)

C. SAMPA Layer Tracing Performance Evaluation

We assessed the layer tracking capability of the SAMPA algorithm using the results shown in Fig. 7(c) and Fig. 8(b1) and (b2). From original echograms, upper layers are more contrasted and visible than lower layers due to lower signal returns from deeper layers. We, therefore, split each echogram into upper and lower portions from the middle, i.e., approximately at 20 m depth, where the layers' contrast starts dropping for evaluation in terms of percentages of the following: good detected layers (G), i.e., layers that are visually detected by an expert and are automatically detected by SAMPA, including partially detected layers; false detected layers (F), i.e., layers detected by SAMPA, but that are not visually detected by an expert; and missing layers (M), i.e., layers that are visually detected by an expert, but are not automatically detected by SAMPA, as highlighted in Table III. Thus, SAMPA provides a better layer detection probability and a lower false detection probability for upper layers than for deeper layers. In Table III, the global good detected layers' rate G is greater than 80%, which is compatible with the theoretical PDF substantiated in Fig. 4. Our quantitative evaluation showed that, generally, SAMPA has good performance while extracting upper layers, and thus, upper layers were much easier to track within echograms, which was expected due to the attenuation of the radar signal in deeper layers and their low contrast manifested by low variance, as proven by the theoretical PDF in Fig. 4. This quantitative analysis is indicative, since the final extracted layers have to be validated by the user according to its application. There is a possibility of connecting fake segmented layers during the running of the smoothing procedure. That may occur

particularly for bottom layers where the contrast has been lost due to anomalies, including layer compression. That is a typical case where the SAMPA algorithm fails by vertically connecting nearby segmented layers. Fake layer connection, however, occurs when there are missing segmented layers within vertically $2\Delta y$ across the echogram. Hence, considering individual layers, fake segmented-layer connection are manageable by the end user according to the final scientific application.

1) *Parameters' Sensitivity and Performance Behavior*: The detection of peaks in the DRT domain is a crucial step in the SAMPA algorithm. It encompasses the peak's amplitude and width detection. The reliability of the resulting maximum spot map, from which the backward DRT is computed, depends on that step to produce extracted layers. Thus, the detection of peaks uses two threshold parameters PTV and PWD to highlight peaks in the DRT domain. Consequently, false detections in the final result mainly come from the tuning of those two parameters. Therefore, it is necessary to analyze the sensitivity of PVT and PWD on performance measures G, F, and M. In particular, we would like the percentage of false detected layers F to be low or at least constant for a given set of PVT and PWD values. Plots of percentages of good detected layers, of false detected layers, and of missing layers versus PWD are shown in Fig. 9(a1)–(c1), respectively, for the echogram in Fig. 7(a), for different values of PVT. In addition, similar plots versus PVT are shown in Fig. 9(a2)–(c2), respectively, for the same echogram, for different values of PWD. Percentages of good detected layers in Fig. 9(a1) increase for different values of PVT as PWD increases, and they stay constant in Fig. 9(a2) as PVT increases for different values of PWD.

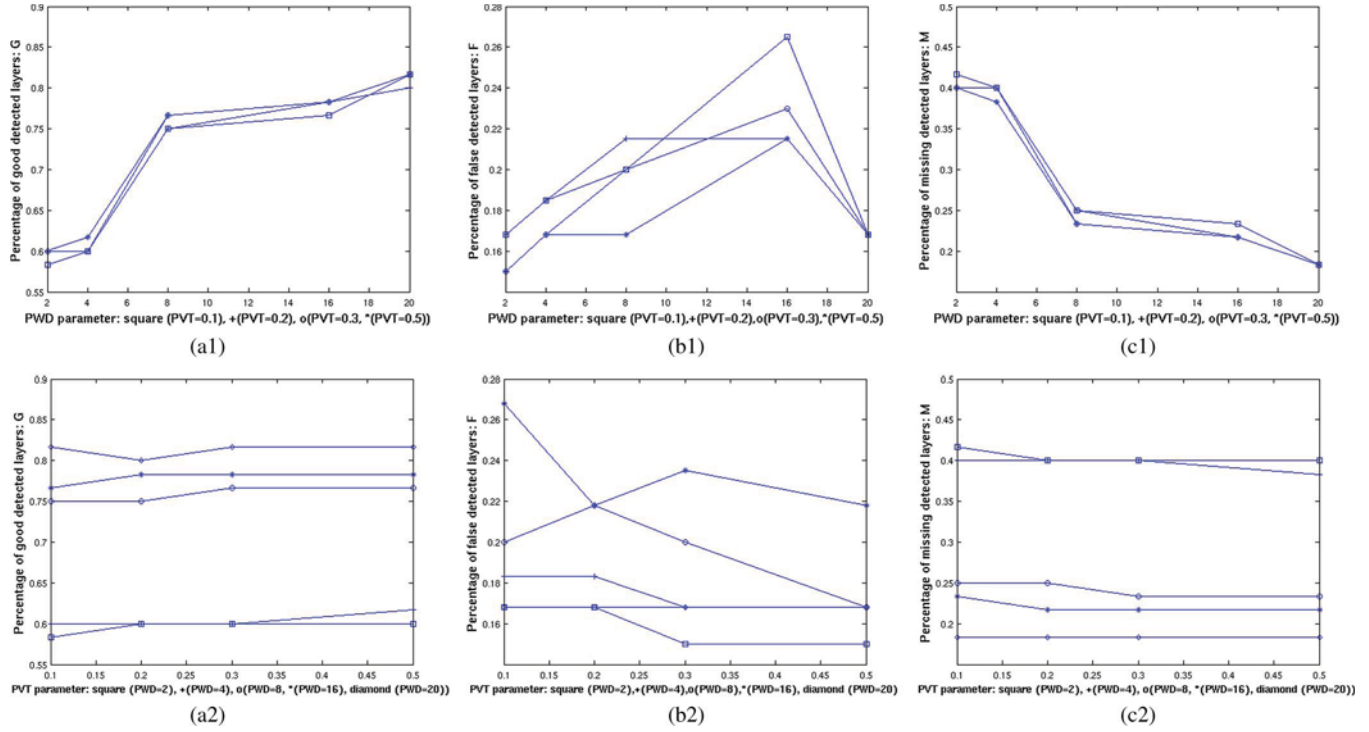


Fig. 9. Parameters' sensitivity and performance behavior. Echogram in Fig. 7(a) was used to analyze the sensitivity of parameters PVT and PWD for the performance behavior. For different values of PVT, as PWD increases: (a1) percentages of good detected layers (G); (b1) percentages of false detected layers (F); (c1) percentages of missing detected layers (M). As PVT increases and for different values of PWD: (a2) percentages of good detected layers (G); (b2) percentages of false detected layers (W); (c2) percentages of missing detected layers (M). In (a1), percentages of good detected layers increase for different values of PVT as PWD increases, and in (a2), they stay constant as PVT increases for different values of PWD. In (b1) and (b2), percentages of false detected layers stay roughly within [15%, 27%], for whichever PVT or PWD increases for different values of either PWD or PVT. In (c1), percentages of missing detected layers decrease for different values of PVT as PWD increases, and in (c2), they are constant when PVT increases for different values of PWD. This analysis substantiates that the SAMPA algorithm has a quasi-constant false detection rate relatively to visually detected layers by an expert, below 20% in general, and that overall performances are good for the following settings: PWD = 20 and PVT $\in [0.1, 0.5]$, for which the detection rate is around 80%.

Percentages of false detected layers stay roughly within [15%, 27%] for whichever PVT or PWD increases for different values of either PWD or PVT in Fig. 9(b1) and (b2). Percentages of missing detected layers decrease in Fig. 9(c1) for different values of PVT as PWD increases, and they are constant in Fig. 9(c2) as PVT increases for different values of PWD. This analysis substantiates that the SAMPA algorithm has a quasi-constant false detection rate, below 20% in general, and that overall performances are good for the following settings: PWD = 20 and PVT $\in [0.1, 0.5]$, for which the detection rate is around 80%.

2) *Trackability of Good Extracted Layers*: One of the ultimate purposes of a layer extraction is the trackability of the resulting layers, i.e., being able to follow each individual layer across wide. In practice, two scenarios occur.

- In an ideal scenario, extracted layers do not cross, and we have a perfect extraction, as shown in Fig. 10(a1). If we weigh each extracted layer point to one unit, the sum of extracted layer points for each column is identical to the number of layers, as illustrated in Fig. 10(b1). The resulting characteristic appears horizontally, meaning perfect trackability of extracted layers.
- In a common scenario, extracted layers may cross, may carry false detection, or may have missing detection, or local anomalies, as shown in Fig. 10(a2). In this case, the sum of extracted layer points for each column is different

to the number of layers, as illustrated in Fig. 10(b2). The resulting characteristic displays downward extrema, meaning lack of perfect trackability of extracted layers.

We have the characteristic of layer trackability (COT) as $COT = \sum_{c \in \text{column numbers}} L(:, c)$, where L corresponds to the array of extracted layer points, where each layer point weighs one unit. Here, the way to interpret COT is *about how well good detected layers are trackable?*, knowing that there exists few false detections.

Understanding COT interpretation is simple, but defining a COT index $iCOT$, i.e., an index of goodness of good detected layers' trackability, that tells whether extracted layers are well trackable or not across wide is a hard task. Indeed, such a COT index interpretation must take into account additional information including a global criterion, such as good and false detection rates, to avoid fully trackable layers but maybe made only of false layers; but also a local criterion such as measure of trackability per column wide across the echogram given the possibility that layers may cross, or that there are local anomalies leading to partly detected layers that are independent of false detection rate.

Hence, we define here the low bound of COT index $iCOT_{\text{Min}}$ by

$$iCOT_{\text{Min}} = \frac{\text{Min}_{COT}}{\text{Max}_{COT}} \in [0, 100\%] \quad (9)$$

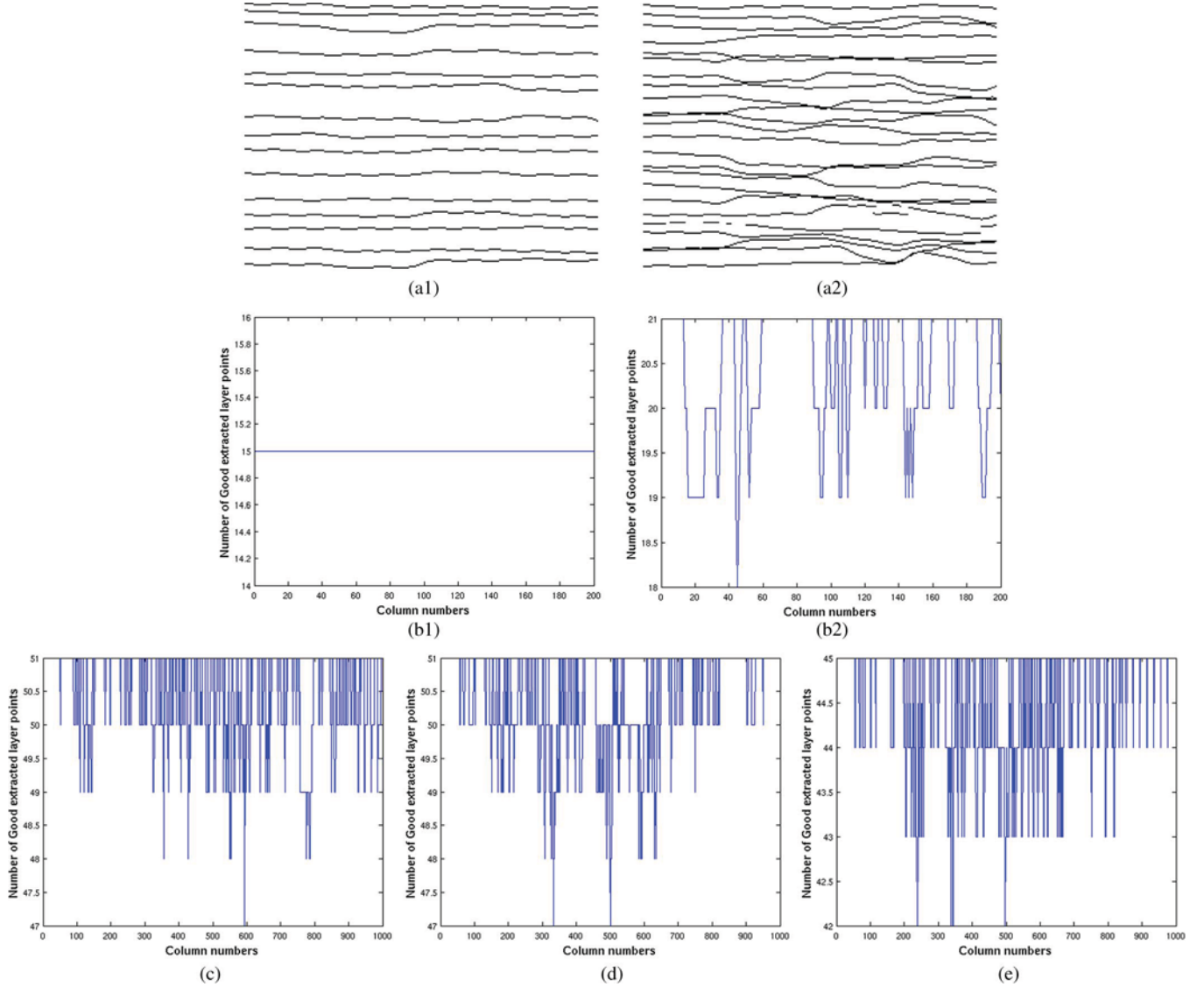


Fig. 10. COT: Here, only good detected layers were considered. (a1) Ideal scenario, a piece of extracted layers with perfect detection. (a2) Common scenario, a piece of extracted layers with crossing layers. (b1) COT from (a1) is a horizontal line, meaning perfect trackability, the characteristic of layer tracking index $iCOT_{Min} = 100\%$, $iCOT_{Avg} = 100\%$, and the validation criterion of $iCOT$, $VC_{COT} = 100\%$. Here, ideal case $\#F = 0$. (b2) COT from (a2) appears with downward extrema (upside-down pyramid), meaning lack of perfect trackability, $VC_{COT} = 87.5\%$, $iCOT_{Min} = 85.7\%$, $iCOT_{Avg} = 97.62\%$; here, $\#F = 3 \neq 0$. (c) COT in Fig. 7(c) ($VC_{COT} = 83\%$, $iCOT_{Min} = 92\%$, $iCOT_{Avg} = 98.95\%$, $\#F = 10$). (d) COT in Fig. 8(a2) ($VC_{COT} = 83\%$, $iCOT_{Min} = 92\%$, $iCOT_{Avg} = 98.85\%$, $\#F = 10$). (e) COT in Fig. 8(b2), ($VC_{COT} = 75\%$, $iCOT_{Min} = 93\%$, $iCOT_{Avg} = 98.98\%$, $\#F = 17$). Values of $iCOT \leq 100\%$ are due to crossing, or missing good detected layers, and we have a relatively good trackability index. More than 90% of good detected layers are trackable, as highlighted in Fig. 11.

where Min_{COT} and Max_{COT} represent the minimum and the maximum of the COT's values, respectively. We also define the average of COT index $iCOT_{Avg}$ by

$$iCOT_{Avg} = \frac{Avg_{COT}}{Max_{COT}} \in [0, 100\%] \quad (10)$$

where Avg_{COT} corresponds to the average of the COT's values column wide. COT here is computed only for $L(:, c)$ representing good detected layers. Therefore, any decrease of either $iCOT_{Min}$ or $iCOT_{Avg}$ comes from artifacts, including crossing or missing parts of good detected layers. Either (9) or (10) is dependent of the existence of the aforementioned artifacts. Indeed if just a column of good detected layers in $L(:, c)$ is full

of zeroes, $iCOT_{Min} = 0$, saying that we face bad trackability. However, $iCOT_{Avg}$ will be different to 0 as long as there are good detected layers. In the same spirit, one crossing of good detected layers decreases $iCOT_{Min}$. However, in the meantime, a good detected layer rate may be great, and in an operational stand point, layers with few missing detected points on columns or few crossings can still be trackable. Thus, $iCOT_{Min}$ gives the worst scenario, whereas $iCOT_{Avg}$ gives average behavior of $iCOT$.

Therefore, either (9) or (10) is not meaningful alone for all detection result scenarios. They are more meaningful in the case of a perfect trackability of good detected layers or for an individual COT's column. However, an individual COT's columns by themselves are less significant for a global interpretation

TABLE IV
BEHAVIORS OF THE VALIDATION CRITERION OF VC_{COT} , COT
MINIMUM INDEX $iCOT_{Min}$, COT AVERAGE INDEX $iCOT_{Avg}$,
AND FALSE DETECTION RATE F FOR THE THREE ECHOGRAMS
PROCESSED IN THE CURRENT STUDY. $iCOT_{Min}$ VALUES
CORRESPOND TO WORST SCENARIOS, WHEREAS
 $iCOT_{Avg}$ VALUES REPRESENT AVERAGE BEHAVIORS

	Data 03 Echogram 0008	Data 03 Echogram 0020	Data 02 Echogram 0068
VC_{COT}	83%	83%	75%
$iCOT_{Min}$	92%	92%	93%
$iCOT_{Avg}$	98.95%	98.85%	98.98%
F	10(17%)	10(17.5%)	17(28%)

of goodness of trackability of good detected layers. We need an additional criterion that captures layer detection global performance first and then uses it to validate the interpretation of either (9) or (10). If we define a validation criterion (i.e., layer detection global performance) VC_{COT} as

$$VC_{COT} = \frac{\#G}{\#G + \#F} \in [0, 100\%] \quad (11)$$

where $\#G$ and $\#F$ represent the number of good detected layers and the number of false detected layers, respectively. In an ideal scenario, given in Fig. 10(b1), $\#F = 0$, $VC_{COT} = 100\%$, $Min_{COT} = Max_{COT}$, $iCOT_{Min} = 100\%$, and $iCOT_{Avg} = 100\%$; otherwise, as shown in Fig. 10(b2), $\#F = 3 \neq 0$, $VC_{COT} = 87.5\%$, $Min_{COT} \leq Max_{COT}$, $iCOT_{Min} = 85.7\%$, and $iCOT_{Avg} = 97.62\%$; both $iCOT_{Min}$ and $iCOT_{Avg}$ are less than 100%, meaning lack of perfect trackability. The higher the values of VC_{COT} and $iCOT_{Min,Avg}$, the more meaningful $iCOT_{Min,Avg}$ will be. $iCOT_{Min,Avg}$ denotes either $iCOT_{Min}$ or $iCOT_{Avg}$. For a general validation purpose and based on performances given in Table III, if we set up $VC_{COT} \geq 70\%$, which means F would be small enough ($< 30\%$) and G would be high enough ($\geq 70\%$), then the use of $iCOT_{Min,Avg}$ as a trackability index in conjunction with VC_{COT} would be meaningful. COTs for good detected layer results in Figs. 7(c), 8(b1), and (b2) are depicted in Fig. 10(c)–(e), respectively.

Based on our assumption (only good detected layers with few short missing parts and few crossings are considered for a meaningful $iCOT_{Min,Avg}$), the corresponding (VC_{COT} , $iCOT_{Min}$, $iCOT_{Avg}$, F) values are given in Table IV. Values of VC_{COT} , $iCOT_{Min}$, and $iCOT_{Avg}$ are less than 100%, due to some crossing or missing parts of good detected layer points. Some layers may partly split by the end of the echogram, whereas others may partly join by the beginning of the echogram. That affects VC_{COT} , $iCOT_{Min}$, $iCOT_{Avg}$, and F behaviors.

COT plots resemble upside-down pyramids [see Fig. 10(b2)–(e)] showing different levels of Min_{COT} values. Min_{COT} values depend on the presence of artifacts more than Max_{COT} . If Max_{COT} values are considered $\#level = 0$, the closer the $\#level$ to Max_{COT} values, the higher the $iCOT_{Min}$. The further the $\#level$ to Max_{COT} values, the lower the $iCOT_{Min}$, as the trackability of good detected layers becomes more sensitive to artifacts, as illustrated in Fig. 11. Thus, for the three examples presented in this paper, more than 90% of good extracted layers are trackable across wide, with a

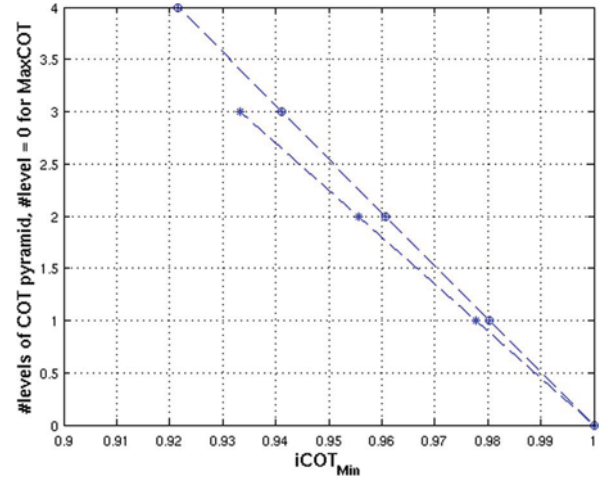


Fig. 11. $iCOT_{Min}$ versus #levels of COT pyramid in Fig. 10(c) (+), Fig. 10(d) (o), and Fig. 10(e) (*). If Max_{COT} values are considered $\#level = 0$, the closer the $\#level$ to Max_{COT} values, the higher the $iCOT_{Min}$. The further the $\#level$ to Max_{COT} values, the lower the $iCOT_{Min}$, as the trackability of good detected layers becomes more sensitive to artifacts, including crossing and missing parts of good detected layers.

good detection rate VC_{COT} greater than 70%. Layers in our area of interest are roughly flat; hence, our approximation of applying the DRT over small blocks holds. As we highlighted it in Section III-A, the DRT maps linear feature radiometry into peaks in the DRT domain where the detection operates. Remote sensing information carries uncertainty when it comes to distinguishing features. Similar features do not necessarily carry identical radiometry values. That uncertainty in either manual or automatic interpretation leads to false or missing detection. Automatic interpretation methods try to minimize the false and missing detection rates. Although a smoothing procedure may introduce some false detections, it is also necessary to connect some segments of layer features that have lost parts and that are still trackable across the echogram. False detections, however, need to be minimized.

D. Example of Application of SAMPA's Outputs: Accumulation Estimation

The SAMPA algorithm was applied to a radar echogram collected coincidentally with the SEAT10-1 ice core located approximately 20 km from the WAIS divide camp [54]. The SAMPA-picked layers were converted from radar travel time into firm depth, using densities collected from the ice core. The SAMPA algorithm was run over each radar trace (≈ 20 cm along track), and then, peaks in range bin picks were averaged to every 100 and 1000 traces to reduce small-scale spatial variability, as described in step #5 (see Section IV-E). For this application, continuous layers of kilometers are considered annual events and not small-scale variability. At core site SEAT10-1, the closest 10 000 traces (≈ 2 km) were used to determine the radar-derived age-depth scale reducing small-scale noise. Error bars are $\pm 1\sigma$ of the 1000 trace picks, to capture the natural layer variation around the core site. The σ is ± 1 standard deviation of the derived accumulation in water equivalent (W.E.). Accumulation is derived using the snow

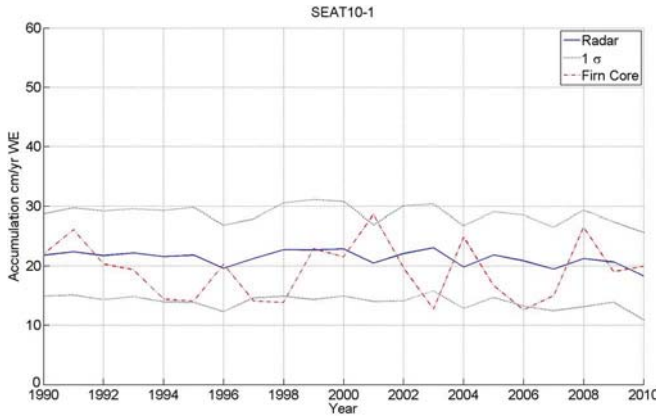


Fig. 12. Accumulation rate (in centimeters) of W.E. per year derived from radar layers picked using the SAMPA algorithm and derived from the SEAT 10-1 ice core [54], showing nearly identical accumulation rates given the estimated 1σ error. The σ is ± 1 standard deviation of the derived accumulation in W.E. Accumulation is derived using the snow density and radar travel time to the SAMPA picks. The mean and standard deviation come from SAMPA picks of each radar trace, which are then averaged across the entire radar echogram grid, which is ≈ 30 km in length for a single year. The error bars are the same distance, i.e., $\pm 1\sigma$ in a single year, but the σ does change from year to year, depending on the SAMPA picks for that year and, ultimately, the snow structure (i.e., Some snow layers (or years) have more or less small-scale variability on an individual trace level, leading to larger and smaller σ values from year to year, when averaged over the entire echogram. For instance, a windier year would likely have formed sastrugi; therefore, more variability in picks and accumulation rates formed point to point (trace to trace) than a calmer year with a flatter snow surface that was buried and imaged.) The differences between the ice core and the radar are larger on a year-to-year basis than expected. This is due to the difference in the type of measurements.

density and radar travel time to the SAMPA picks. The mean and standard deviation come from SAMPA picks of each radar trace, which are then averaged across the entire radar echogram grid, which is ≈ 30 km in length for a single year. The spatial average of traces over the echogram ensures that the summer season annual layer (dominating layer) is picked and not the high-spatial-variability noise from small-scale snow processes. The error bars are the same distance, i.e., $\pm 1\sigma$ in a single year, but the σ does change from year to year, depending on the SAMPA picks for that year and, ultimately, the snow structure (i.e., Some snow layers (or years) have more or less small-scale variability on an individual trace level, leading to larger and smaller σ values from year to year, when averaged over the entire echogram. For instance, a windier year would likely have formed sastrugi; therefore, more variability in picks and accumulation rates formed point to point (trace to trace) than a calmer year with a flatter snow surface that was buried and imaged.). The accumulation rate derived from the SAMPA-picked layers and the ice core at SEAT10-1 are nearly identical, as shown in Fig. 12.

The differences between the ice core and the radar are larger on a year-to-year basis than expected. This is due to the difference in the type of measurements (the radar and ice cores are different measurements; the radar is measuring the yearly peak in density, whereas the ice core is measuring water isotope peak). Further study is needed to understand the difference between the yearly peak in density and the isotopic peak, and that goes outside the scope of this paper, but over the long term, both measurement averages should converge as shown here.

VI. SUMMARY

A SAMPA algorithm for ice-sheet radar echograms has been presented. The SAMPA algorithm computes the DRT of ice-sheet radar echograms by blocks to overcome undulation behavior of firn layers along track. The resulting DRT domain carries point sums, i.e., spot peaks representing firn layers, that are much easier to extract than in the original space. We applied two thresholds (amplitude and width of the peaks) to highlight peaks in the RT domain. The backward RT was then computed for each corresponding block to get back firn segmented layers into their original space. The resulting segmented layers were rough and discontinuous. We used a regularization procedure to connect and smooth them and to achieve the final layer tracing. The overall trackability of good detected layers is greater than 90%. The SAMPA algorithm has been tested on near-surface radar echograms collected by the IceBridge Ku-band radar and on ground-based data collected during the 2010 SEAT traverse. Firn layers in the area are roughly flat, which leads to making use of the RT to extract them. Once the parameters are trained and set, SAMPA is fully automated and is capable of tracking 1000 km of firn layers from radar echograms.

With respect to the data sets (relatively flat layers) that were processed, SAMPA extracted upper layer features better than deeper layer features due to low signal returns from attenuation and subsequent low layers' contrast below 20 m depth. SAMPA-picked layers when compared to the SEAT10-1 ice core show that the algorithm is capable of determining layers once trained well enough to give nearly identical accumulation rates to a coincident ice core measurement. The SAMPA algorithm is more efficient for picking multiple firn layers than previous manual approaches and can be used for a variety of scientific studies, including deriving accumulation rates from near-surface radars.

Our future work will be focusing on reducing false and missing detections by 1) managing uncertainty in the detection of peaks in the DRT domain via threshold parameters and 2) by taking into account underlying radiometry values of the echogram in the smoothing procedure.

APPENDIX I

DERIVATION OF THE THEORETICAL PDF OF THE DISTRIBUTION OF THE RT DOMAIN

The DRT domain is made with point sum values $s_i = N \sum_{n=1}^{L_0} p_n$, where p_n are pixel intensities of the original echogram space, L_0 is the length of integration used to compute the DRT, and N is the number of elementary summations $\sum_{n=1}^{L_0} p_n$ along a linear feature (see Fig. 1). Each p_n value follows the log-normal law. $\mathcal{L}(x|\mu_l, \sigma_l) = (1/x\sigma_l\sqrt{2\pi}) \exp(-((\ln(x) - \mu_l)^2/2\sigma_l^2))$, where μ_l and σ_l represent the mean and the standard deviation, respectively. Therefore, a point sum s_i in the DRT domain follows the sum of log-normal distributions. An exact analytical expression of the PDF of the sum of log-normal random variables is, however, still an unsolved question.

Using the following assumption: *Within a block, pixels belonging to a given segmented layer have close intensity values*

p_0 ; therefore, a point sum in the DRT domain can be approximated by $s_i = N \sum_{n=1}^{L0} p_n \approx N \cdot L0 \cdot p_0$. It becomes much easier to assess the PDF h of s_i . We have

$$\begin{aligned} \text{From the echogram distribution, } p_n &\sim \mathcal{L}(p < 0 | \mu_l, \sigma_l) \\ &= \frac{1}{p\sigma_l\sqrt{2\pi}} \exp\left(-\frac{(\ln(p) - \mu_l)^2}{2\sigma_l^2}\right). \end{aligned} \quad (12)$$

$$\begin{aligned} \text{From the DRT domain distribution, } s_i &\sim h_{\{s_i, N, L0, \mu_l, \sigma_l\}}(p) \\ &= \frac{1}{N \cdot L0} \mathcal{L}\left(\frac{p}{N \cdot L0} > 0 | \mu_l, \sigma_l\right) \\ &= \frac{1}{p\sigma_l\sqrt{2\pi}} \exp\left(-\frac{(\ln(\frac{p}{N \cdot L0}) - \mu_l)^2}{2\sigma_l^2}\right) \end{aligned} \quad (13)$$

where μ_l and σ_l represent the mean and the standard deviation of the echogram data, respectively.

From (5), the probability of detecting peaks Pdp in the DRT domain is then given by

$$\begin{aligned} Pdp &= \int_{DRT_{\max 1}}^{DRT_{\max 2}} \mathcal{H}(m) dm \\ &= \int_{DRT_{\max 1}}^{DRT_{\max 2}} N_{DRT} h(m) \left[\int_0^\infty h(m) dm \right]^{N_{DRT}-1} dm \quad (14) \\ &= \frac{N_{DRT}}{2} \left[\operatorname{erf}\left(\frac{\ln(\frac{DRT_{\max 2}}{N \cdot L0}) - (\mu_l + \sigma_l^2)}{\sigma_l \sqrt{2}} + \frac{\sigma_l}{\sqrt{2}}\right) \right. \\ &\quad \left. - \operatorname{erf}\left(\frac{\ln(\frac{DRT_{\max 1}}{N \cdot L0}) - (\mu_l + \sigma_l^2)}{\sigma_l \sqrt{2}} + \frac{\sigma_l}{\sqrt{2}}\right) \right] \end{aligned} \quad (15)$$

where N_{DRT} is the number of points (i.e., point sum s_i) in the DRT domain, $\operatorname{erf}(x)$ represents the error function defined by $\operatorname{erf}(x) = (2/\sqrt{\pi}) \int_0^x \exp(-t^2) dt$, and $[DRT_{\max 1}, DRT_{\max 2}]$ is the range of integration. Note that

$$\begin{aligned} &\left[\int_0^\infty h(m) dm \right]^{N_{DRT}-1} \\ &= \left[\left(\frac{1}{2} \operatorname{erf}\left(\frac{\ln(\frac{p}{N \cdot L0}) - (\mu_l + \sigma_l^2)}{\sigma_l \sqrt{2}} + \frac{\sigma_l}{\sqrt{2}}\right) \right) \right]_0^\infty^{N_{DRT}-1} = 1. \end{aligned}$$

Fig. 3 depicts the theoretical probability of detecting peaks Pdp in the DRT domain for $N_{DRT} = 50 \times 50$ point sums, $N = 10$, $L0 = 5$, and the range of point sums containing peaks in the DRT domain $[DRT_{\max 1} = 10^9, DRT_{\max 2} = 10^{10}]$. On a given segmented layer within a block, the Pdp increases as σ_l increases and $Pdp > 0.8$, for $\sigma_l = 10^3$, for the range of point sums used for the simulation. This analysis substantiated that high signal return echoes (i.e., with high variance of segmented-layer points) contribute to a high detectability of peaks in the DRT domain.

APPENDIX II SEGMENTED-LAYER FEATURES' SMOOTHING ALGORITHM USED IN SAMPA

Let sl be an extracted segmented-layer feature, which carries roughnesses and maybe some missing points due to the absence of signal returns or other artifacts. The smoothing algorithm [51] estimates the final smoothed layer fl from the extracted segmented-layer sl using the following iterative scheme:

$$fl\{k+1\} = IDCT(\Gamma \times DCT(W(sl - fl\{k\}) + fl\{k\})) \quad (16)$$

where

- DCT and $IDCT$ denote discrete cosinus and inverse discrete cosinus transforms, respectively;
- k represents the current iteration;
- Γ a diagonal matrix denoted the tensor defined by

$$\Gamma_{i,j} = \begin{cases} \left[1 + s(2 - 2\cos((i-1)\pi/n))\right]^{-1}, & \text{if } i = j \\ 0, & \text{if } i \neq j; \end{cases} \quad (17)$$

- W the bisquare weights defined by [55]

$$W_i = \begin{cases} (1 - (u_i/4.685)^2)^2, & \text{if } |u_i/4.685| < 1 \\ 0, & \text{if } |u_i/4.685| \geq 1 \end{cases} \quad (18)$$

where $u_i = r_i[1.4826\text{MAD}(r)]$
 $\sqrt{1 - (\sqrt{1 + \sqrt{1 + 16s}})/(\sqrt{2}\sqrt{1 + 16s})}^{-1}$, $r_i = rl_i - fl_i$ represents the residual of the i th observation, MAD denotes the median absolute deviation (see [56]), and $r = rl - fl$;

- $GCV(s)$ denotes the generalized cross-validation used to estimate the smoothing parameter s defined by [57]

$$GCV(s) = \frac{|W^{1/2}(fl - rl)|^2 / (n - n_{\text{miss}})}{(1 - \text{Tr}(H)/n)^2} \quad (19)$$

where n represents the number of elements of rl ;

- $\text{Tr}(H)$ denotes the matrix trace of H defined by $\text{Tr}(H) = \sum_{i=1}^n [1 + s(2 - 2\cos((i-1)\pi/n))]^{-1}$, where $H = (I_n + sD^T D)^{-1}$ denotes the hat matrix, and D a tridiagonal square matrix defined by [58] as $D_{i,i-1} = 2/(h_{i-1}(h_{i-1} + h_i))$, $D_{i,i} = -2/(h_{i-1}h_i)$, and $D_{i-1,i} = 2/(h_i(h_{i-1} + h_i))$, $h_i = \sqrt{1 + \sqrt{1 + 16s}}/(\sqrt{2}\sqrt{1 + 16s})$ denotes the step between $fl\{k\}$ and $fl\{k+1\}$.

In practice, less than ten iterations are sufficient to get an acceptable smoothing result.

ACKNOWLEDGMENT

The authors would like to thank anonymous reviewers for their comments, remarks, suggestions, and questions raised throughout the reviewing process and that significantly improved the quality of the manuscript, as well as the CReSIS teams for collecting and processing raw data and for their excellent support. Some data used in this paper were acquired by NASA's Operation IceBridge Project.

REFERENCES

- [1] A. Macqueen, *Radio echo-sounding as a glaciological technique: A bibliography*. Cambridge, U.K.: World Data Centre 'C' for Glaciol., Scott Polar Res. Inst., Univ. of Cambridge, 1988.
- [2] S. Gogineni *et al.*, "High-resolution mapping of near-surface internal snow layers with a wideband radar," in *Proc. 10th Int. Conf. Ground Penetrating Radar*, 2003, vol. 1/2, pp. 769–771.
- [3] F. T. Ulaby, R. K. Moore, and A. D. Fung, *Microwave Remote Sensing, Active and Passive, Radar Remote Sensing and Surface Scattering and Emission Theory*, vol. II. Norwood, MA, USA: Artech House, 1982.
- [4] J. L. Bamber, R. L. Layberry, and S. P. Gogineni, "A new ice thickness and bed data set for the Greenland ice sheet," *J. Geophys. Res.*, vol. 106, no. D24, pp. 33 773–33 780, Dec. 2001.
- [5] H. Conway, B. L. Hall, G. H. Denton, A. M. Gades, and E. D. Waddington, "Past and future grounding-line retreat of the West Antarctic ice sheet," *Science*, vol. 286, no. 5438, pp. 280–283, Oct. 1999.
- [6] T. A. Waddington, E. D. Neumann, M. R. Koutnik, H. P. Marshall, and D. L. Morse, "Inference of accumulation-rate patterns from deep layers in glaciers and ice sheets," *J. Glaciol.*, vol. 53, no. 183, pp. 694–712, Dec. 2007.
- [7] V. Spikes *et al.*, "Variability in accumulation rates from GPR profiling on the West Antarctic plateau," *Ann. Glaciol.*, vol. 39, no. 39, pp. 238–244, Jun. 2005.
- [8] H. Anschütz, A. Sinisalo *et al.*, "Variation of accumulation rates over the last eight centuries on the East Antarctic Plateau derived from volcanic signals in ice cores," *J. Geophys. Res., Atmos.*, vol. 116, no. D20, pp. D20103–1–D20103–12, Oct. 2011.
- [9] L. Koenig, S. Martin, M. Studinger, and J. Sonntag, "Polar airborne observations fill gap in satellite data," *EOS Trans. AGU*, vol. 91, no. 38, pp. 333–334, Sep. 2010.
- [10] B. Panzer *et al.*, "An ultra-wideband, microwave radar for measuring snow thickness on sea ice and mapping near-surface internal layers in polar firn," *J. Glaciol.*, vol. 59, no. 214, pp. 244–254, Apr. 2013.
- [11] S. Gogineni *et al.*, "Polar radar for ice sheet measurements (PRISM)," *Remote Sens. Environ.*, vol. 111, no. 2/3, pp. 204–211, Nov. 2007.
- [12] T. Rink, P. Kanagaratnam, D. Braaten, T. Akins, and S. Gogineni, "A wideband radar for mapping near-surface layers in snow," in *Proc. IEEE IGARSS*, 2006, pp. 3655–3657.
- [13] W. J. Van de Berg, M. R. Van den Broeke, C. H. Reijmer, and E. van Meijgaard, "Reassessment of the Antarctic surface mass balance using calibrated output of a regional atmospheric climate model," *J. Geophys. Res.*, vol. 111, no. D11, pp. D11104–1–D11104–15, Jun. 2006.
- [14] J. Ettema *et al.*, "Higher surface mass balance of the Greenland ice sheet revealed by high-resolution climate modeling," *Geophys. Res. Lett.*, vol. 36, no. 12, pp. L12501–1–L12501–5, Jun. 2009.
- [15] J. T. M. Lenaerts, M. R. Van den Broeke, W. J. Van de Berg, E. Van Meijgaard, and P. Kuipers Munneke, "A new, high-resolution surface mass balance map of Antarctica (1979–2010) based on regional atmospheric climate modeling," *Geophys. Res. Lett.*, vol. 39, no. 4, pp. L04501–1–L04501–5, Feb. 2012.
- [16] D. Bromwich, A. Nicolas, and J. Monaghan, "An assessment of precipitation changes over Antarctica and the Southern Ocean since 1989 in contemporary global reanalyses," *J. Clim.*, vol. 24, no. 16, pp. 4189–4209, Aug. 2011.
- [17] R. I. Cullather and M. G. Bosilovich, "The energy budget of the polar atmosphere in MERRA," *J. Clim.*, vol. 25, no. 1, pp. 5–24, Jan. 2012.
- [18] E. Hanna *et al.*, "Greenland ice sheet surface mass balance 1870 to 2010 based on twentieth century reanalysis, and links with global climate forcing," *J. Geophys. Res., Atmos.*, vol. 116, no. D24, Dec. 2011.
- [19] L. S. Koenig, E. J. Steig, D. P. Winebrenner, and C. A. Shuman, "A link between microwave extinction length, firn thermal diffusivity, and accumulation rate in West Antarctica," *J. Geophys. Res., Earth Surface*, vol. 112, no. F3, pp. F03018–1–F03018–10, Sep. 2007.
- [20] O. Eisen *et al.*, "Ground-based measurements of spatial and temporal variability of snow accumulation in East Antarctica," *Rev. Geophys.*, vol. 46, no. 2, pp. RG2001–1–RG2001–39, Jun. 2008.
- [21] W. Dierking, S. Linow, and W. Rack, "Toward a robust retrieval of snow accumulation over the Antarctic ice sheet using satellite radar," *J. Geophys. Res., Atmos.*, vol. 118, no. 8, p. 3258, Apr. 27, 2013.
- [22] M. B. Lythe and D. G. Vaughan, "Bedmap: A new ice thickness and subglacial topographic model of Antarctica," *J. Geophys. Res., Solid Earth*, vol. 106, no. B6, pp. 11 335–11 351, Jun. 2001.
- [23] K. Müller *et al.*, "An 860 km surface mass-balance profile on the East Antarctic plateau derived by GPR," *Ann. Glaciol.*, vol. 51, no. 55, pp. 1–8, Jun. 2010.
- [24] M. Fahnestock, W. Abdalati, S. Luo, and S. Gogineni, "Internal layer tracing and age-depth-accumulation relationships for the northern Greenland ice sheet," *J. Geophys. Res.*, vol. 106, no. D24, pp. 33 789–33 797, Dec. 2001.
- [25] K. Matsuoka, A. Gades, H. Conway, G. Catania, and C. F. Raymond, "Radar signatures beneath a surface topographic lineation near the outlet of Kamb Ice Stream and Engelhardt Ice Ridge, West Antarctica," *Ann. Glaciol.*, vol. 50, no. 51, pp. 98–104, Aug. 2009.
- [26] CRESIS, Center for Remote Sensing of Ice Sheets (CREGIS), Dec. 2012. [Online]. Available: <ftp://data.cresis.ku.edu/data/picker/>
- [27] G. J. Freeman, A. C. Bovik, and J. V. Holt, "Automated detection of near surface martian ice layers in orbital radar data," in *Proc. IEEE SSIAI*, May 2010, pp. 117–120.
- [28] L. C. Sime, R. C. A. Hindmarsh, and H. Corr, "Instruments and methods automated processing to derive dip angles of englacial radar reflectors in ice sheets," *J. Glaciol.*, vol. 57, no. 202, pp. 260–266, Apr. 2011.
- [29] P. Rockett, "The accuracy of sub-pixel localisation in the Canny edge detector," in *Proc. Brit. Mach. Vis. Conf.*, 1999, pp. 392–401.
- [30] A. Ferro and L. Bruzzone, "Automatic extraction and analysis of ice layering in radar sounder data," *IEEE Trans. Geosci. Remote Sens.*, vol. 51, no. 3, pp. 1622–1634, Mar. 2013.
- [31] S. Arcone, V. Spikes, and G. Hamilton, "Stratigraphic variation within polar firn caused by differential accumulation and ice flow: Interpretation of a 400 MHz short-pulse radar profile from West Antarctic," *J. Glaciol.*, vol. 51, no. 174, pp. 407–422, Jun. 2005.
- [32] C. Richardson, E. E. Aarholt, S. E. Hamran, P. Holmlund, and E. Isaksson, "Spatial distribution of snow in Western Dronning Maud Land, East Antarctica, mapped by a ground-based snow radar," *J. Geophys. Res., Solid Earth*, vol. 102, no. B9, pp. 20 343–20 353, Sep. 1997.
- [33] H. P. Marshall and G. Koha, "FMCW radars for snow research," *Cold Regions Sci. Technol.*, vol. 52, no. 2, pp. 118–131, Apr. 2008.
- [34] K. Langley *et al.*, "From glacier facies to SAR backscatter zones via GPR," *IEEE Trans. Geosci. Remote Sens.*, vol. 46, no. 9, pp. 2506–2516, Sep. 2008.
- [35] R. L. Hawley *et al.*, "ASIRAS airborne radar resolves internal annual layers in the dry-snow zone of Greenland," *Geophys. Res. Lett.*, vol. 33, no. 4, pp. L04502–1–L04502–5, Feb. 2006.
- [36] V. P. Onana, E. Trouvé, G. Mauris, J. P. Rudant, and E. Tóny, "Detection of linear features in synthetic-aperture radar images by use of the localized Radon transform and prior information," *Appl. Opt.*, vol. 43, no. 2, pp. 264–273, Jan. 2004.
- [37] J. Canny, "A computational approach to edge detection," *IEEE Trans. Pattern Anal. Mach. Intell.*, vol. PAMI-8, no. 6, pp. 679–714, Nov. 1986.
- [38] R. Touzi, A. Lopes, and P. Bousquet, "A statistical and geometrical edge detector for SAR images," *IEEE Trans. Geosci. Remote Sens.*, vol. 26, no. 6, pp. 764–773, Nov. 1988.
- [39] F. Tupin, H. Matre, J. F. Mangin, J. M. Nicolas, and E. Pechersky, "Detection of linear features in SAR images: Application to road network extraction," *IEEE Trans. Geosci. Remote Sens.*, vol. 36, no. 2, pp. 434–453, Mar. 1998.
- [40] G. Beylkin, "Discrete Radon transform," *IEEE Trans. Acoust., Speech, Signal Process.*, vol. 35, no. 2, pp. 162–172, Feb. 1987.
- [41] A. C. Copeland, G. Ravichandran, and M. M. Trivedi, "Localized Radon transform-based detection of ship wakes in SAR images," *IEEE Trans. Geosci. Remote Sens.*, vol. 31, no. 1, pp. 35–45, Jan. 1995.
- [42] G. Darche, "Spatial interpolation using a fast parabolic transform," in *Proc. 60th Annu. Int. Meet., Soc. Explor. Geophys., Expanded Abstr.*, 1990, pp. 1647–1650.
- [43] J. R. Thorson and J. F. Claerbout, "Velocity-stack and slant-stack stochastic inversion," *Geophysics*, vol. 50, no. 12, pp. 2727–2741, Dec. 1985.
- [44] S. R. Deans, *The Radon Transform and Some of Its Applications*. New York, NY, USA: Wiley, 1983.
- [45] A. Papoulis and S. Unnikrishna Pillai, *Probability, Random Variables and Stochastic Process*, 4th ed. New York, NY, USA: McGraw-Hill, 2002.
- [46] B. C. Armstrong and H. D. Griffiths, "CFAR detection of fluctuating targets in spatially correlated K-distributed clutter," *Proc. Inst. Elec. Eng.—Radar Signal Process.*, vol. 138, no. 2, pp. 139–152, Apr. 1991.
- [47] C. Tison, J.-M. Nicolas, F. Tupin, and H. Maitre, "A new statistical model for Markovian classification of urban areas in high-resolution SAR images," *IEEE Trans. Geosci. Remote Sens.*, vol. 42, no. 10, pp. 2046–2057, Oct. 2004.
- [48] A. Ferro and L. Bruzzone, "Analysis of radar sounder signals for the automatic detection and characterization of subsurface features," *IEEE Trans. Geosci. Remote Sens.*, vol. 50, no. 11, pp. 4333–4348, Nov. 2012.

- [49] G. Marsaglia, W. Tsang, and J. Wang, "Evaluating Kolmogorov's distribution," *J. Stat. Softw.*, vol. 8, no. 18, pp. 1–4, 2003.
- [50] S. Kullback *et al.*, "Letter to the editor: The Kullback-Leibler distance," *The Amer. Stat.*, vol. 41, no. 4, pp. 340–341, 1987.
- [51] D. Garcia, "Robust smoothing of gridded data in one and higher dimensions with missing values," *Comput. Stat. Data Anal.*, vol. 54, no. 4, pp. 1167–1178, Apr. 2010.
- [52] S. Gogineni, T. Chuah, C. Allen, K. Jezek, and R. K. Moore, "An improved coherent radar depth sounder," *J. Glaciol.*, vol. 44, no. 148, pp. 659–669, 1998.
- [53] C. Leuschen, G. Prasad, R. Fernando, J. Paden, and C. Allen, "IceBridge Ku-Band radar L1B geolocated radar echo strength profiles [03/26/2010]," Nat. Snow Ice Data Center, Boulder, CO, USA, 2010, Digital media.
- [54] L. K. Burgener *et al.*, "An observed negative trend in West Antarctic accumulation rates from 1975 to 2010 evidence from new observed and simulated records," *J. Geophys. Res.*, vol. 118, no. 10, pp. 4205–4216, May 27, 2013.
- [55] R. M. Heiberger and R. A. Becker, "Design of an S function for robust regression using iteratively reweighted least squares," *J. Comput. Graph. Stat.*, vol. 1, no. 3, pp. 181–196, Sep. 1992.
- [56] P. J. Rousseeuw and C. Croux, "Alternatives to the median absolute deviation," *J. Amer. Stat. Assoc.*, vol. 88, no. 424, pp. 1273–1283, Dec. 1993.
- [57] P. Craven and G. Wahba, "Smoothing noisy data with spline functions. Estimating the correct degree of smoothing by the method of generalized cross-validation," *Numer. Math.*, vol. 31, no. 4, pp. 377–403, Mar. 1978.
- [58] W. C. Yueh, "Eigenvalues of several tridiagonal matrices," *Appl. Math. E-Notes*, vol. 5, pp. 66–74, 2005.



Vincent de Paul Onana received the Ph.D. degree with Highest Distinction in 2001 from the University Paris-Est/Marne-la-Vallee, France, working in the field of geoinformation extraction from satellite remote sensing images, and the M.Sci. degree in electrical engineering in 2014 from the New York University Polytechnic School of Engineering, New York, NY, USA.

Since 2010, he has been with the Cryospheric Sciences Laboratory, NASA Goddard Space Flight Center, Greenbelt, MD, USA, delivering support to

NASA's Operation IceBridge. He is also with ADNET Systems Inc., Lanham, MD, USA. He has been involved in teaching activities and scientific research projects overseas. He has coauthored several communications and publications in the area of automating feature extraction from remote sensing data. His research interests include automatic interpretation of passive and active remote sensing image/signal applied to spatial risk assessment, land, coastal, tropical rain forest, urban environments, and currently polar ice environments.



Lora S. Koenig received the M.S. degree in geography from the University of Utah, Salt Lake City, UT, USA, in 2003 and the Ph.D. degree in geophysics from the University of Washington, Seattle, WA, USA, in 2008.

In 2008, she joined the Cryospheric Sciences Laboratory, NASA Goddard Space Flight Center, Greenbelt, MD, USA, where she is currently a Physical Scientist. She has spent over 12 months conducting field experiments on the ice sheets of Greenland and Antarctica for satellite validation studies, including

leading a field traverse in West Antarctica. Her research interests include satellite remote sensing of snow and ice, passive and active microwave remote sensing, and understanding the surface mass balance of ice sheets.



Julia Ruth is an undergraduate at the University of Maryland, College Park, MD, USA due to receive her B.S. in Physics in May of 2014. From June 2012 to August 2012, she completed an internship in the Cryospheric Sciences Laboratory, NASA Goddard Space Flight Center, Greenbelt, MD, USA.

Since October 2012, she has been with the Earth System Science Interdisciplinary Center at the University of Maryland based at the NOAA Laboratory for Satellite Altimetry, College Park, MD, USA, completing an internship in remote sensing of sea ice. Her research interests include active remote sensing, signal processing, and polar climate change. In April 2014 she received a National Science Foundation Graduate Fellowship.



Michael Studinger received the Ph.D. degree in 1998 from the Alfred Wegener Institute for Polar and Marine Research, Bremerhaven, Germany.

He is the Project Scientist for NASA's Operation IceBridge Mission. He is with the NASA's Goddard Space Flight Center, Greenbelt, MD, USA. His research interests include physical processes in polar regions, linking tectonics, ice sheet dynamics, and life in extreme environments, such as subglacial lakes. He is using integrated sets of aerogeophysical data, including gravity, magnetics, ice-penetrating

radar, and laser altimeter measurements to answer key questions in solid Earth geophysics and glaciology. His main research projects focus on the role of subglacial environment in a global framework.



Jeremy P. Harbeck received the B.S. degree in atmospheric sciences from the University of Washington, Seattle, WA, USA, in 2006. He is currently working toward the M.S. degree in geophysics at the University of Alaska Fairbanks, Fairbanks, AK, USA.

He is currently with ADNET Systems Inc., Lanham, MD, USA, delivering as science support for NASA's Operation IceBridge Program, with a focus on the development and production of sea ice freeboard and thickness products. He is also with

the Cryospheric Sciences Branch (Code 615), NASA Goddard Space Flight Center, Greenbelt, MD, USA. He has participated in multiple field deployments throughout the Arctic and Antarctic.